JGR Atmospheres

RESEARCH ARTICLE
10.1029/2024JD042643

Day-Night and Land-Sea Contrasts of Upscale Convective Growths at Coastal South China

Lin Su[1,2], Lanqiang Bai[3], Sijia Zhang[4], Guixing Chen[1,2], and Yu Du[1,2]

[1]School of Atmospheric Sciences, Sun Yat-sen University, and Southern Marine Science and Engineering Guangdong Laboratory (Zhuhai), Zhuhai, China, [2]Key Laboratory of Tropical Atmospheric-Ocean System, Ministry of Education, Zhuhai, China, [3]Foshan Tornado Research Center, Guangdong-Hong Kong-Macao Greater Bay Area Academy of Meteorological Research, Foshan, China, [4]National Institute of Natural Hazards, Ministry of Emergency Management of China, Beijing, China

Key Points:

- Convection initiation arises from near-surface convergence, and upscale convective growth is the result of large-scale deep upward motions
- Convective cells initiated over land tend to grow upscale during the daytime, whereas those over sea are more likely to develop at night
- Daytime convections initiated over sea are the least likely to develop, yet produce the most intensive rainfall

Correspondence to:
L. Su and Y. Du,
sulin8@mail.sysu.edu.cn;
duyu7@mail.sysu.edu.cn

Citation:
Su, L., Bai, L., Zhang, S., Chen, G., & Du, Y. (2025). Day-night and land-sea contrasts of upscale convective growths at coastal South China. *Journal of Geophysical Research: Atmospheres*, *130*, e2024JD042643. https://doi.org/10.1029/2024JD042643

Received 10 OCT 2024
Accepted 28 APR 2025

Abstract Upscale convective growth (UCG) is the key stage for heavy rainfall production within the life cycle of a mesoscale convective system (MCS). The precise prediction of heavy rainfall hinges upon a comprehensive understanding and accurate representation of UCG dynamics. This study investigates the characteristics of pre-summer UCG at coastal South China (CSC), and uncovers noteworthy diurnal and land-sea disparities in UCG at CSC. Convective cells initiated over land tend to grow upscale during the daytime, whereas those triggered over sea surface are more likely to develop at night. Compared with convection initiation, which is closely associated with boundary-layer convergence, UCG relies upon large-scale deep vertical motion in the atmosphere. Environmental dynamic conditions play a dominant role in promoting the UCGs at CSC. The key environmental factors include low-level jet, low-level vortex/shearline, mid-level westerly jet, and vertical wind shear. Nocturnal convective cells triggered over the sea surface demonstrate the greatest likelihoods of upscale growth due to the lower prerequisites for additional environmental conditions for their upscale developments. The MCSs stemming from these convective cells generate the lightest rainfall among all MCSs initiated at CSC. Conversely, daytime convective cells initiated over sea surface and nocturnal convections initiated over land, particularly the former, necessitate exceptionally favorable environmental conditions for their developments, and thus exhibit low probability to grow upscale. The MCSs developed from daytime convective cells initiated over sea surface produce the most intensive rainfall in CSC.

Plain Language Summary Accurate prediction of heavy rainfall depends on thorough understanding and precise representation of the key stages during the development of a mesoscale convective system. Being the transition stage from an isolated deep moist convection into a mesoscale convective system, upscale convective growth (UCG) is the critical phase to heavy rainfall production during the life cycle of a mesoscale convective system. Based on a multi-year radar reflectivity observation, this study attempts to provide well-documented spatiotemporal characteristics of the pre-summer UCG in coastal South China (CSC). Furthermore, the key environmental factors that play crucial roles in UCG in the region are identified. The results unveil the importance of deep vertical motion for newly initiated convections to develop and summarize the dynamic and thermodynamic environmental conditions required for the upscale growth of daytime and nocturnal convections initiated over land and sea surface of CSC.

1. Introduction

Upscale convective growth (UCG) is the transition from isolated deep moist convection into mesoscale convective systems (MCSs), which is the key stage to the occurrence of heavy rainfall and severe weather hazards, such as flooding and damaging winds (Houze Jr, 2004; Mulholland et al., 2019). Despite the importance of UCG in the occurrence of heavy rainfall, it is indicated to be the least understood and poorly forecasted portion in the convective lifecycle of heavy rainfall, and thus remains an ongoing challenge for heavy rainfall prediction (Thielen & Gallus, 2019).

Previous studies demonstrate that many environmental conditions play important roles in promoting the evolution of convective cells once they are triggered, including enhanced heat and moisture fluxes and instability (Coniglio et al., 2011; Zhang et al., 2021), strong low-level convergence at the exits of low-level jets (Dial et al., 2010; Du, Chen, Han, Mai, et al., 2020; French & Parker, 2010; Shen et al., 2020; Zhang et al., 2021), low-level vortex/shearlines (Shen et al., 2020), upper-level negative geostrophic potential vorticity (Coniglio et al., 2011), vertical

wind shear (Weisman & Trapp, 2003; Zhang et al., 2021), and orography or orography-induced gravity waves (Coniglio et al., 2011; Du, Chen, Han, Bai et al., 2020; Mulholland et al., 2019; Zhang et al., 2021). Internal processes of convective cells also significantly affect the occurrence of UCGs. Cold pools produced by convective cells may spread laterally and interact with neighboring cold pools, encouraging secondary convection initiations (CI) and promoting UCG (Du, Chen, Han, Bai et al., 2020; Hiris & Gallus, 2021; Mulholland et al., 2019; Squitieri & Gallus, 2022; Yang et al., 2021; M. Zhang et al., 2022). Some numerical studies suggest that upscale-growing MCSs can self-organize through surface-based cold pools and internal processes, regardless of external environmental influences (Parker, 2021; Schumacher & Peters, 2017; Trapp & Weisman, 2003).

Coastal South China (CSC) is one of the key regions of frequent heavy rainfall events in China (Ding, 1992). Being a coastal region characterized by monsoonal climate, rainfall in CSC is significantly influenced by the activity of East Asian monsoon. During May–June, a large amount of warm and moist air is transported from the tropical ocean to CSC by the South China Sea summer monsoon, resulting in frequent heavy rainfall events (Chen et al., 2011; Li et al., 2020; Luo et al., 2020). This period, namely the pre-summer rainy season, accounts for ∼50% of the total annual rainfall in CSC. Pre-summer heavy rainfall in CSC is mostly associated with MCSs (Chen et al., 2022, 2024; Li et al., 2021; Liu et al., 2018; Zhang et al., 2024). Thorough understanding and precise representation of the evolution and key stages of MCSs in CSC are crucial for accurate prediction of pre-summer heavy rainfall in the region (Huang & Luo, 2017; Luo et al., 2020; Shen et al., 2020).

CI in CSC has been intensively studied recently, and the characteristics, key environment conditions and local factors to CI in the region have been well documented in numerous observational analyses and numerical studies (Bai et al., 2020a, 2020b, 2021; Bao et al., 2021; Du & Chen, 2019; Du, Chen, Han, Bai et al., 2020; Du, Chen, Han, Mai et al., 2020; Luo et al., 2020; Mai & Du, 2022; Su et al., 2023; Wang et al., 2024; Zeng et al., 2023; S. Zhang et al., 2022; Zhu et al., 2021). However, studies on UCG in the region are relatively rare and mostly case studies (Du, Chen, Han, Bai et al., 2020; Du, Chen, Han, Mai et al., 2020; Li et al., 2013; Liu et al., 2018; Wang et al., 2014). Statistical studies mainly focus on mature stage of MCSs (Chen et al., 2022; Li et al., 2021; Meng et al., 2013). Our understanding on the factors favorable for an initiated convective cell to grow upscale is still limited. Based on a multi-year radar reflectivity observation and an in-depth comparison between CI events with and without UCG, this study attempts to address the following two questions: (a) What are the spatiotemporal characteristics of the pre-summer UCG in CSC in a climatological manner; (b) what are the key environmental factors that play crucial roles in UCG in the region?

The remainder of the manuscript is organized as follows: the data and methods used for the study are introduced in Section 2, the characteristics of UCGs in CSC are presented in Section 3, with the key environmental factors and dynamic processes for UCGs in CSC discussed in Section 4, and the conclusions are given in Section 5.

2. Methodology

2.1. UCG Identification

Radar reflectivity derived from operational weather radar mosaics over South China during pre-summer (May 1–June 30) from 2013 to 2019 is used for the UCG identification. The radar mosaics were produced by the National Meteorological Center of China Meteorological Administration. The UCG identification is based upon the CI data set of South China provided by Bai et al. (2020a, 2020b), in which a CI is defined as the first occurrence of a convective cell with maximum reflectivity ≥40 dBZ. Only the pristine CIs are included in this data set. A pristine CI has to meet one of the following two conditions: (a) No pixel above 25 dBZ was observed 30 min prior to the candidate convective cell within 60 km of the current position of the cell; (b) no pixel reaching 35 dBZ was observed 30 min prior to the candidate convective cell within 60 km of the current position of the cell, and no pixel exceeding 25 dBZ was observed 60 min prior to the candidate convective cell within 100 km of the current position of the cell.

In this study, CIs triggered within a distance of 100 km from the coast of South China (indicated by the red dashed lines in Figure 3a) is tracked for UCG identification. As illustrated by the flow chart in Figure 1, the detected CIs are classified into four categories for further statistics and analysis based on the location and the time of occurrence in a diurnal cycle: (a) CIs occurred over land area during daytime (daytime land-CIs), (b) nighttime (nocturnal land-CIs), (c) over sea area during daytime (daytime sea-CIs), and (d) nighttime (nocturnal sea-CIs).

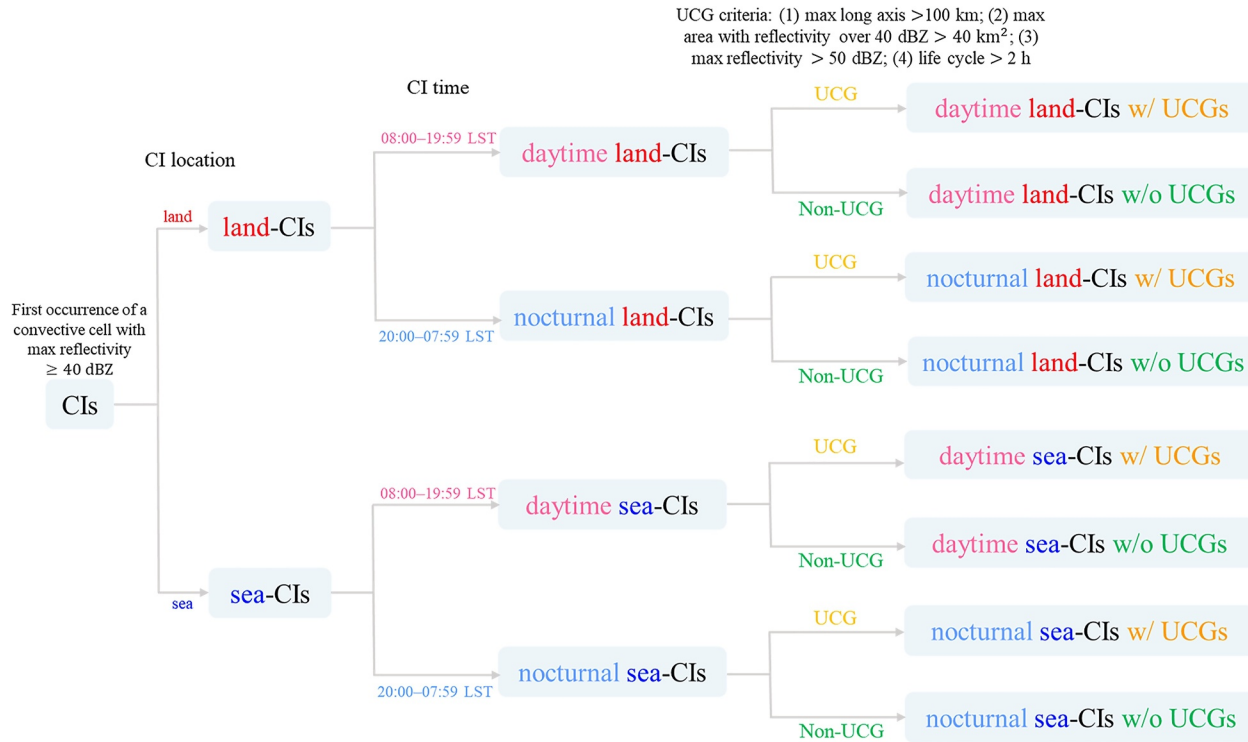

Figure 1. Flow chart illustrating the classification of CIs in CSC.

Specifically, the daytime and nighttime are defined as 08:00–19:59 Local Standard Time (LST), and 20:00–07:59 LST, respectively.

A UCG is detected when a convective cell grows and meets the criteria for MCSs. By referring to Parker and Johnson (2021), Meng et al. (2013), and Li et al. (2021), an MCS is determined if the following criteria are met: (a) The long axis of a convection reaches 100 km; (b) the area with reflectivity over 40 dBZ exceeds 40 km^2; (c) the maximum reflectivity of the convection is over 50 dBZ; (d) the convection lasts for 2 hr or longer since the time of CI. All detected UCGs are manually verified to ensure they can be traced back to a pristine CI in CSC. According to the criteria, the detected CIs in each scenario are further classified into two states, with and without UCGs.

Examples are presented in Figure 2 to demonstrate the evolution of the convective cell from CI to UCG for each scenario. The case for daytime land-CIs is illustrated by Figures 2a and 2b. The convective cell is initiated at land area in the western CSC at 13:50 LST (Figure 2a), then moves northeastward, and grows into an MCS at 16:20 LST, 19 May 2013 (Figure 2b). The case for nocturnal land-CIs is presented in Figures 2c and 2d. In this case, the convective cell is triggered on the east coast of the Pearl River Delta (PRD) at 0:20 LST (Figure 2c), and develops into an MCS at 3:20 LST, 16 May 2013 in a quasi-stationary state (Figure 2d). The case for daytime sea-CIs is displayed in Figures 2e and 2f. The convective cell emerges at the sea surface off the west coast of CSC at 14:00 LST (Figure 2e), and grows into an MCS at 15:40 LST, 6 June 2016,while moving northeastward (Figure 2f). The case for nocturnal sea-CIs is shown in Figures 2g and 2h. The convective cell is initiated at the sea surface off the coast of the west coast of CSC at 1:00 LST (Figure 2g), and develops into an MCS at 4:50 LST, 24 May 2013 while moving northeastward (Figure 2h).

The characteristics of rainfall associated with CI events in different categories are examined based on rainfall observations from the integrated multi-satellite retrievals for global precipitation measurement (IMERG). The rainfall observations are with horizontal and temporal resolutions of 8 km and 30 min, respectively (Huffman et al., 2015). Note that the rainfall associated with CI events indicates the accumulated rainfall within a 3-hr window since the time of CI for each event. Additionally, only the rainfall within the range of the convective cells associated with the detected CIs is considered as the rainfall caused by the corresponding event, therefore,

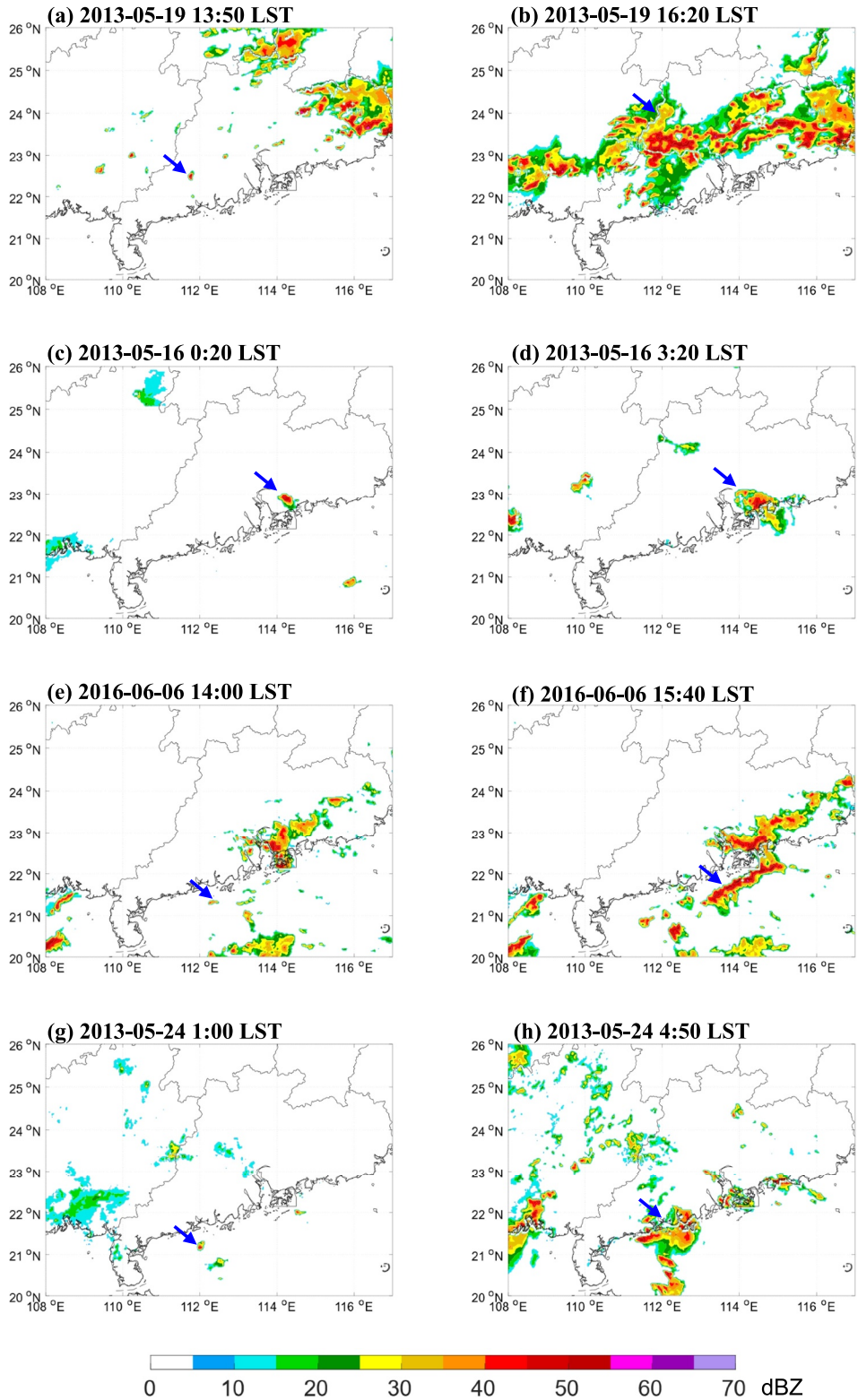

Figure 2. Evolution from convection initiations to upscale convective growth for daytime land-CIs (a–b), nocturnal land-CIs (c–d); daytime sea-CIs (e–f), and nocturnal sea-CIs (g–h). The blue arrow indicates the tracked convective storm.

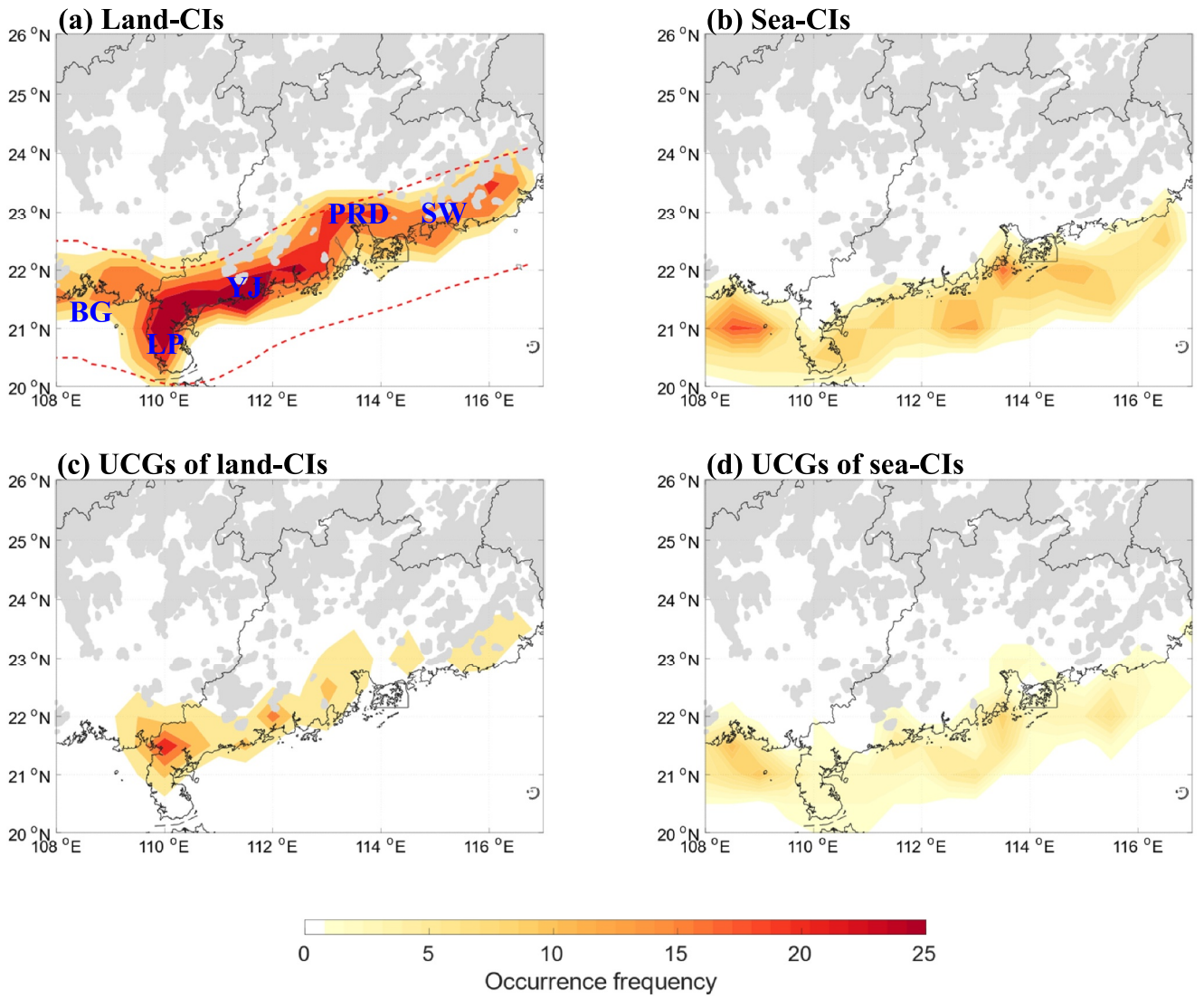

Figure 3. Occurrence frequency of land-CIs (a), sea-CIs (b), UCGs of land-CIs (c), and sea-CIs (d) with topography higher than 300 m (gray shading) at coastal South China.

the rainfall occurred out of the range of the concerned convective cells is masked in the processing of IMERG data to exclude the influences of irrelevant convective cells.

2.2. UCG-Associated Meteorological Conditions

The fifth generation of the European Center for Medium-Range Weather Forecasts Atmospheric Reanalysis (ERA5) data set with a horizontal resolution of 0.25° at a time interval of 1 hr are used for investigating the UCG-associated background meteorological conditions. The ERA5 combines great amounts of historical observations into global estimates using advanced modeling and data assimilation systems (Hersbach et al., 2020), and has been demonstrated to perform markedly better compared to its coarser-resolution predecessors (He et al., 2021; Q. Jiang et al., 2021; Y. Jiang et al., 2021; Jiang, Han, et al., 2021; B. Liu et al., 2021; L. Liu et al., 2021; Song & Wei, 2021). A number of studies have been conducted to comprehensively examine the applicability of the ERA5 in representing historical meteorological fields, including temperature (Chao et al., 2020; Tang et al., 2021; Zou et al., 2022), wind (Chen et al., 2021; Y. Jiang et al., 2021; Liu et al., 2022), moisture (W. Zhang et al., 2019; Y. Zhang et al., 2019), precipitation fields (Q. Jiang et al., 2021; Jiao et al., 2021; Wu et al., 2022; Xie et al., 2022) in China. These studies demonstrate a good performance of the ERA5 in reproducing the spatiotemporal variability

Table 1
Statistics for UCGs of Daytime Land-CIs (the Second Row), Nocturnal Land-CIs (the Third Row), Daytime Sea-CIs (the Fourth Row), and Nocturnal Sea-CIs (the Fifth Row) in Coastal South China During Pre-Summer of 2013–2019

	Region			
	Land		Sea	
	Time			
Metrics	Daytime	Nocturnal	Daytime	Nocturnal
UCG/CI frequency	276/640 (43%)	94/237 (40%)	56/143 (39%)	133/253 (53%)
CI-UCG time (min)	94	98	100	89
CI-UCG Dist. (km)	58	57	50	56

in meteorological fields across most regions of China, including South China, and even outperforms satellite retrievals in some circumstances or regions.

3. Characteristics of Pre-Summer UCGs at CSC

3.1. General Characteristics of UCGs

A total of 876 land-CIs is identified during pre-summer of 2013–2019, out of which 370 are followed by UCGs, accounting for 42% of all land-CIs (Table 1). Figure 3 presents the spatial distributions for UCGs at CSC in pre-summer. The land-CIs shown in Figure 3a exhibit concentrated hotspots extending from the Leizhou Peninsula (LP) to the west coast of the PRD, particularly on the coast or at the windward side of the coastal terrain, such as Yangjiang (YJ) and Shanwei (SW). UCGs of Land-CIs predominantly cluster at the west of CSC, spanning from 110°E to 112°E (Figure 3c), with the center located at LP and YJ. Most of land-CIs with UCGs tend to move northward or northeastward (Figure 4a). As demonstrated in Figure 4c, over 50% of the land-CIs with UCGs move northeastward (including north-northeast, northeast, and east-northeast).

Land-CIs and their UCGs show significant diurnal variations (Figure 5a). The diurnal variation of the land-CIs, whether with or without UCGs, shows consistency with a primary peak occurring at 12 LST. The UCGs of the land-CIs exhibit a primary peak at 15 LST, which is 3 hr later than the primary peak of land-CIs. During the pre-summer of 2013–2019, a total of 640 daytime land-CIs were identified, and 43% of them have underwent a UCG. The mean duration and moving distance from CI to UCG are 94 min and 58 km, respectively, for daytime land-CIs (Table 1). 237 nocturnal land-CIs are detected, and 40% are found to grow upscale. Despite that, the total number of detected nocturnal land-CIs is less than half of daytime land-CIs, the percentage of nocturnal land-CIs that undergo UCGs, as well as the mean duration and moving distance from CI to UCG, are similar to those observed for daytime land-CIs (Table 1).

Comparing to land-CIs, the occurrence frequency of sea-CIs is significantly lower, as illustrated in Figure 3b. A total of 395 sea-CIs is detected during pre-summer of 2013–2019, and 48% of them are followed by UCGs (Table 1). The sea−CI hotspots are primarily located at the sea surface of the Beibu Gulf (BG), the estuary of the PRD and its adjacent sea area. The UCGs of sea-CIs exhibit concentrated hotspots in the BG, as well as the estuary of the PRD and its surrounding area, particularly the west of the coastal PRD (Figure 3d). Unlike the case for land-CIs, most of sea-CIs with UCGs tend to move northeastward or eastward (Figure 4b). Similar to the case for land-CIs with UCGs, approximately 45% of sea-CIs with UCGs have their pathway toward northeast (Figure 4d).

As depicted in Figure 5b, the diurnal variations of sea-CIs and their UCGs are not as pronounced as the land-CIs. Nevertheless, the sea-CIs exhibit a higher occurrence frequency from midnight to early morning (01–06 LST), with a primary peak at 06 LST. The UCGs of sea-CIs demonstrate a higher occurrence frequency at 02–09 LST, which are 1–3 hr later than the peak of sea-CIs. A total of 143 daytime sea-CIs is identified during pre-summer of 2013–2019, and 39% of them are followed by UCGs, exhibiting the smallest likelihood to grow upscale among all scenarios. The mean duration of daytime sea-CIs with UCGs is 100 min from CI to UCG, which is the longest among all scenarios. Note that the moving distances of sea-CIs toward UCGs are generally shorter than those for their counterparts, especially for daytime sea-CIs, the mean moving distance of which is 50 km from CI to UCG, indicating relatively stationary locations for the daytime sea-CIs with UCGs. By contrary, 253 of nocturnal sea-

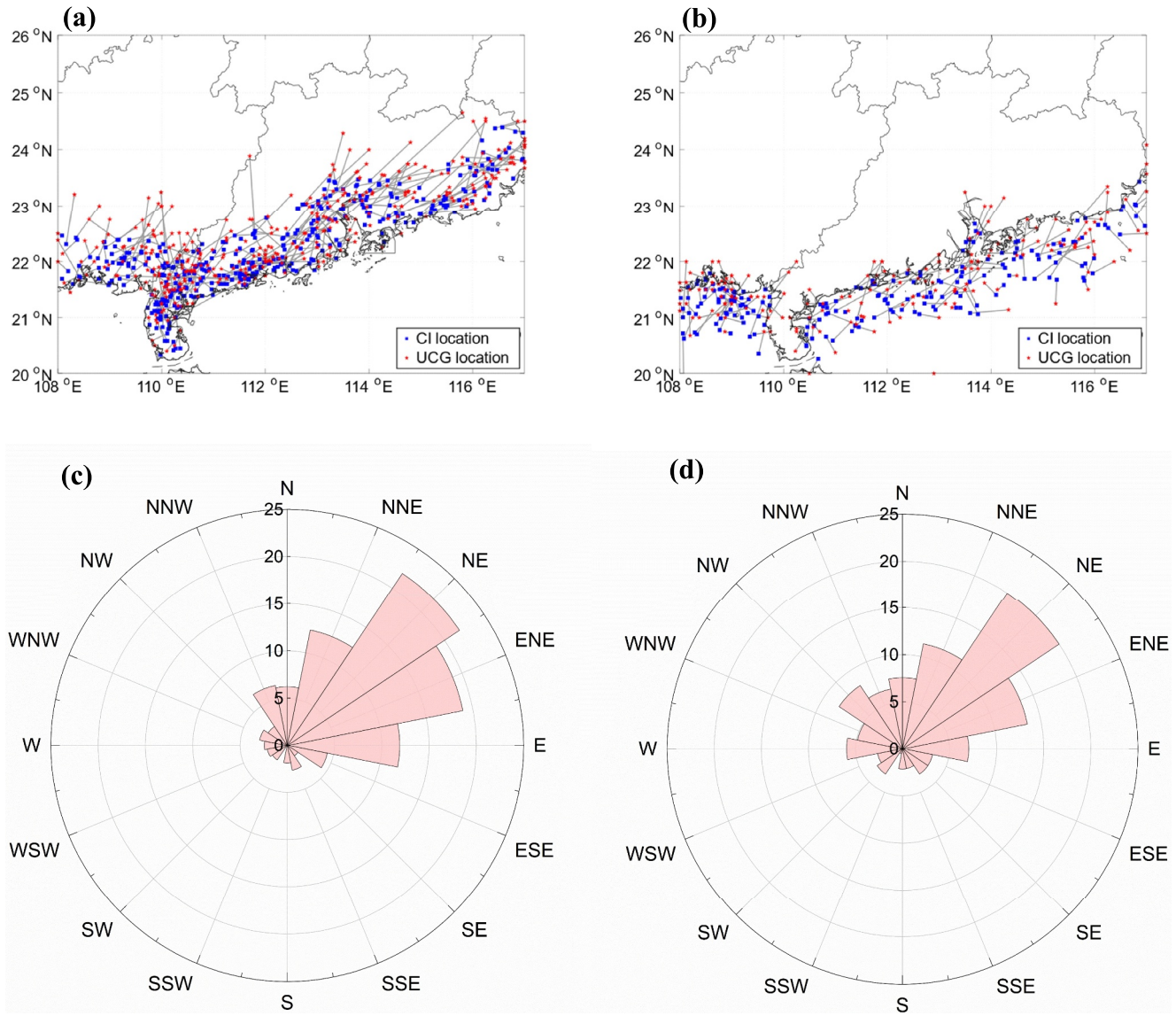

Figure 4. Moving path (upper panel) and windrose map for moving direction (lower panel) for land- (a, c) and sea-CIs (b, d) toward UCGs.

CIs are detected, and 53% of them grow upscale, being the highest percentage among all scenarios. This suggests that nocturnal sea-CIs hold the greatest potential to grow upscale. Meanwhile, nocturnal sea-CIs require a minimum duration of 89 min toward UCGs.

3.2. Characteristics of UCG-Associated Rainfall

Figure 6 illustrates the composites of the total rainfall within a 3-hr window since the occurrence of CIs in various scenarios. For daytime land-CIs without UCGs, the rainfall is only observed in the north of the PRD, with the maximum 3-hr rainfall smaller than 3 mm (Figure 6a). For daytime land-CIs with UCGs, the rainfall is observed over the most area of CSC, and exhibits a significant enhancement with the maximum 3-hr rainfall exceeding 6 mm (Figure 6b). Nocturnal land-CIs without UCGs produce light and scattered rainfall at YJ, SW, and the north of the PRD, with the maximum 3-hr rainfall smaller than 3 mm (Figure 6c). By contrary, the 3-hr rainfall for nocturnal land-CIs with UCGs exhibits three centers at the north of the LP, the northeast of the PRD, and SW, with the maximum of all centers exceeding 6 mm (Figure 6d).

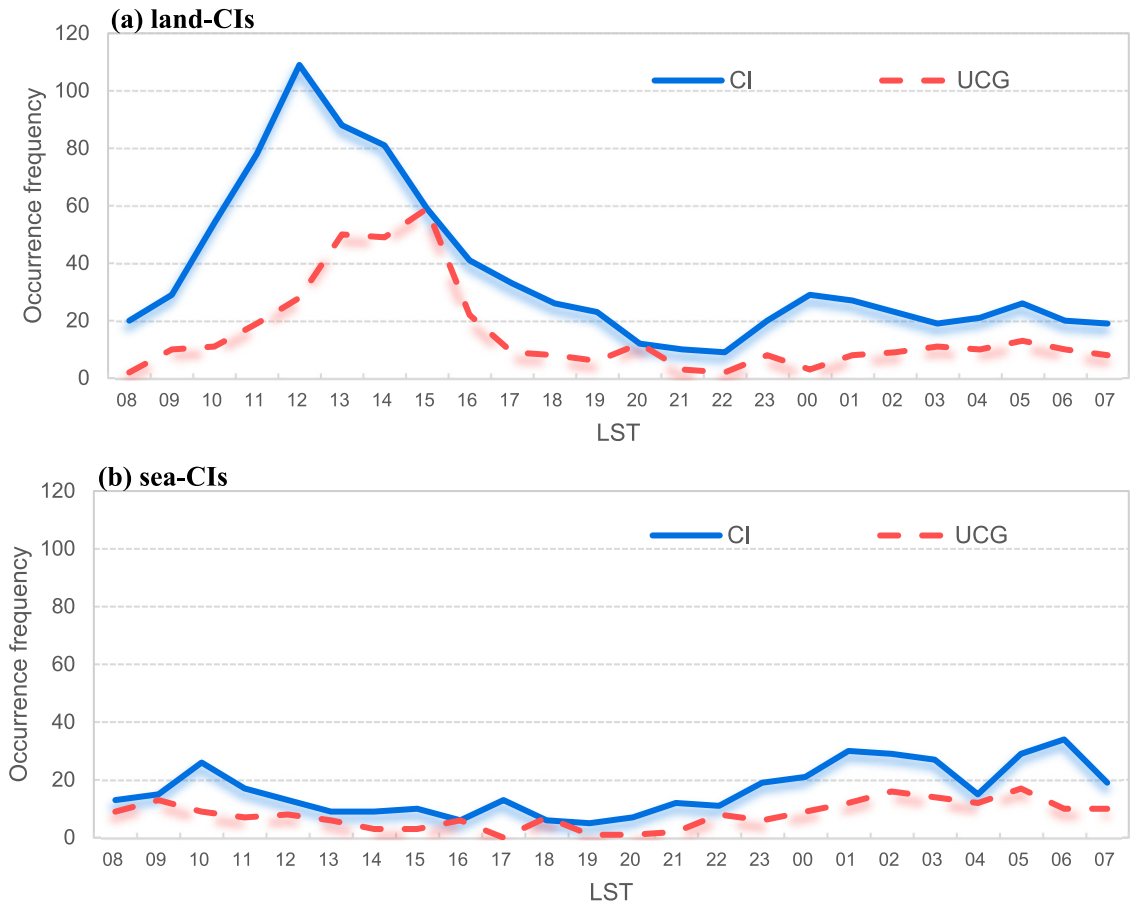

Figure 5. Diurnal variations for land-CIs (a) and sea-CIs (b) at coastal South China.

The rainfall for daytime sea-CIs without UCGs barely produce any rainfall (Figure 6e). The 3-hr rainfall for daytime sea-CIs with UCGs displays a substantial enhancement compared to their counterparts without UCGs, particularly at the east coast of South China; the rainfall center is located at SW and surrounded sea surface, with the maximum exceeding 8 mm, which is the most intensive rainfall among all scenarios for CIs with UCGs (Figure 6f). The rainfall for the nocturnal sea-CIs is observed at the sea surface off the west coast of the PRD, with the 3-hr rainfall smaller than 3 mm (Figure 6g). The 3-hr rainfall for the nocturnal sea-CIs with UCGs showcases an enhancement along the coast of South China (Figure 6h) compared to their counterparts without UCGs, however, this enhancement is less significant when compared to the other three scenarios (Figures 6b–6d and 6f).

In summary, notable diurnal and land-sea disparities are observed in pre-summer UCGs at CSC. Nocturnal sea-CIs exhibit the highest probability to grow upscale, whereas both nocturnal land-CIs and daytime sea-CIs demonstrate the lowest probability. Over 50% of the land-CIs with UCGs and around 45% of the sea-CIs with UCGs move toward northeastward. UCGs of land-CIs peak during the early afternoon, whereas those of sea-CIs increase from midnight and reach their peak in the early morning. UCGs lead to a significant rainfall enhancement in CSC, and the initiation location and occurrence time of convections that grow upscale results distinct rainfall patterns in CSC. UCGs of land-CIs result in rainfall enhancement in both coastal and further inland areas of CSC, whereas UCGs of sea-CIs contribute to rainfall enhancement at the coast. UCGs of the daytime sea-CIs generate the largest rainfall enhancement, whereas UCGs of the nocturnal sea-CIs produce the smallest, in CSC among all scenarios. The dynamic and thermodynamic conditions associated with the UCGs of various scenarios, as well as the related mechanisms in the context of large-scale meteorological conditions, will be discussed in the subsequent section.

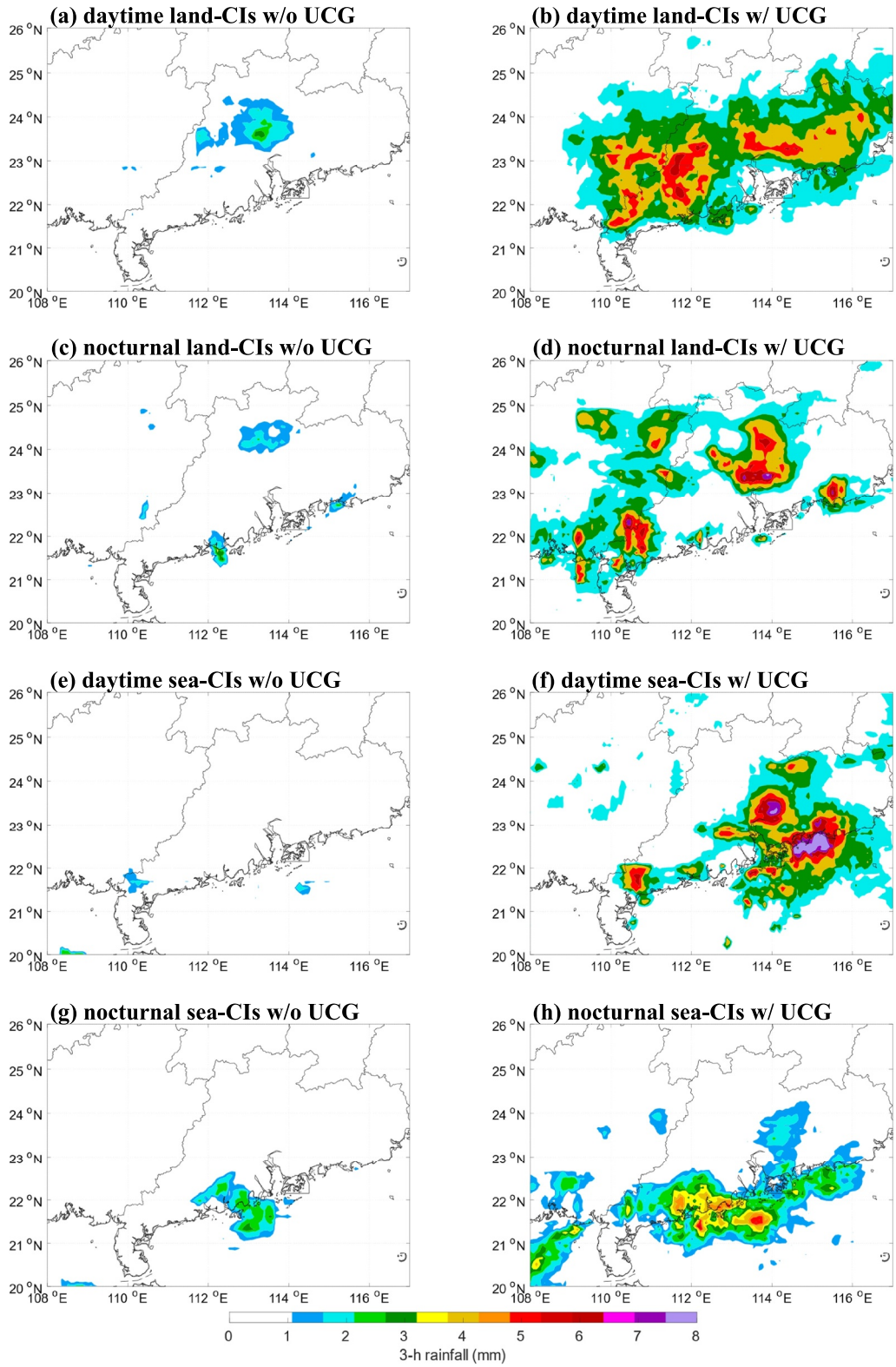

Figure 6. Composite 3-hr rainfall since the occurrence of CIs for daytime and nocturnal land-CIs without (a, c) and with UCGs (b, d) and sea-CIs without (e, h) and with UCGs (f, h) at coastal South China.

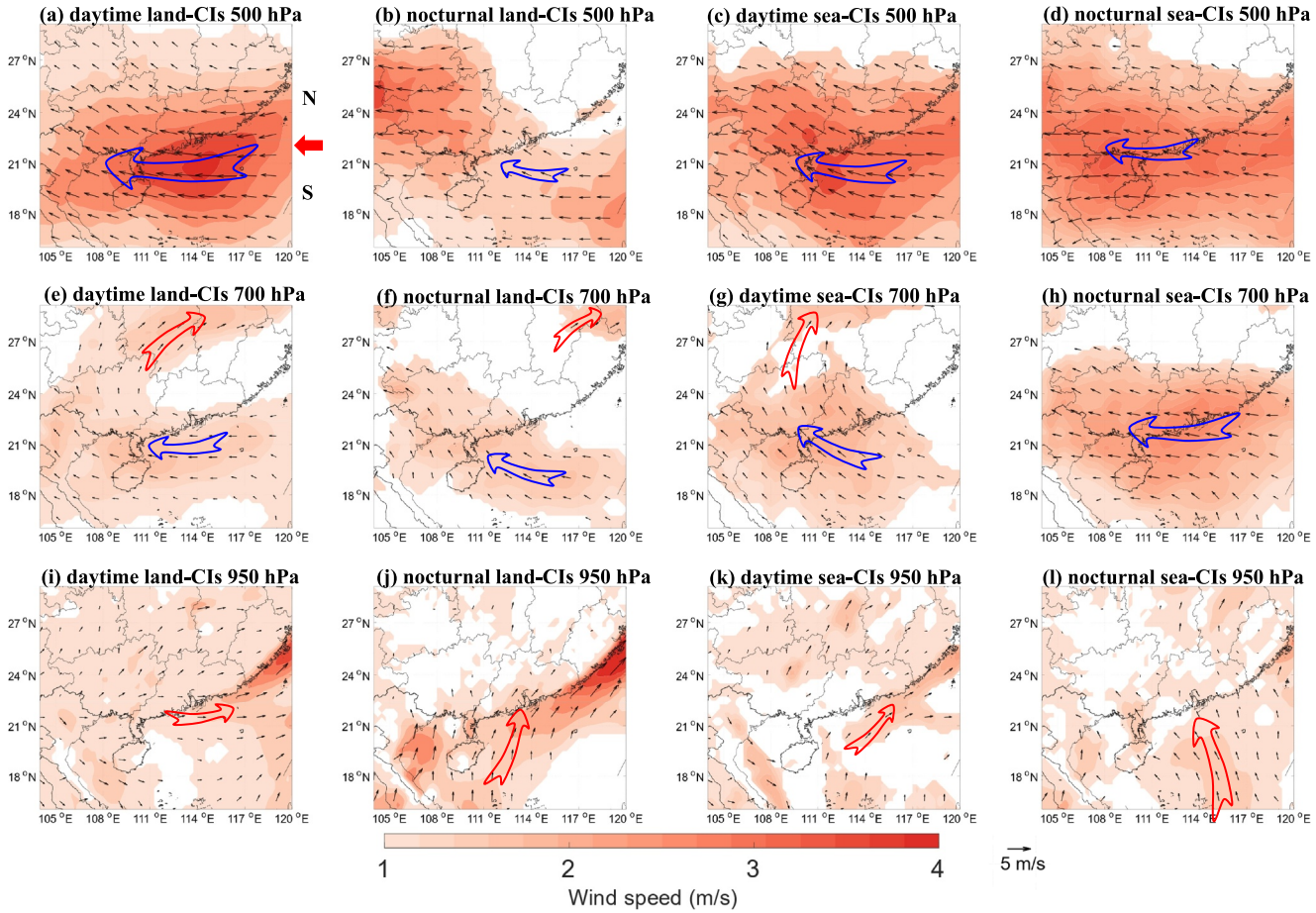

Figure 7. Composite wind difference between CIs without UCGs and pre-summer mean at 500-hPa (upper panel), 700-hPa (middle panel) and 950-hPa (lower panel) over South China for daytime land-CIs (a, e, and i), nocturnal land-CIs (b, f, and j), daytime sea-CIs (c, g, and k), and nocturnal sea-CIs (d, h, and l). The red arrow in panel (a) indicates the boundary (22°N) between the north (N) and south (S) of South China. Shaded colors indicate differences significant at the significance level of 0.01.

4. UCG-Associated Meteorological Conditions

4.1. Dynamics

4.1.1. Horizontal Wind Fields

The composite wind anomalies for various CI-cases without UCGs at 500, 700 and 950-hPa over South China are presented in Figure 7. Specifically, the wind anomalies are at the time 1-hr prior to the occurrence of CIs and relative to the mean pre-summer winds over South China during 2013–2019. CIs/UCGs that coincide with other events within a 3-hr window before or after the event are excluded from the analysis to eliminate any potential influences from adjacent convective events on the meteorological fields.

The 500-hPa wind for CIs without UCGs exhibits easterly anomalies prevailing over South China across various scenarios, particularly at CSC, as indicated by the blue arrows in Figures 7a–7d. This implies a weakened 500-hPa westerly jet and zonal divergence over CSC. The most pronounced 500-hPa easterly anomaly is discernible for daytime land-CIs (Figure 7a), whereas the least significant anomaly is observed for nocturnal land-CIs (Figure 7b). Furthermore, easterly or southeasterly anomalies are identifiable at 700 hPa over the sea surface off the coast of South China, whereas southwesterly anomalies are observed northeast of South China, as presented in Figures 7e–7h. This suggests an anticyclonic anomaly to the east of CSC compared with the mean wind field. The most pronounced anticyclonic anomaly is observed for sea-CIs without UCGs, particularly in the scenario of nocturnal sea-CIs without UCGs (Figure 7h).

Table 2
Regional Mean of Wind Anomalies (m/s) Over the North (N) and South (S) of South China for Various Convection Initiations Scenarios

	Scenario											
	Land-CIs						Sea-CIs					
	Time											
	Daytime			Nocturnal			Daytime			Nocturnal		
	Level											
Component[a]/Region	500 hPa	700 hPa	950 hPa	500 hPa	700 hPa	950 hPa	500 hPa	700 hPa	950 hPa	500 hPa	700 hPa	950 hPa
$(u_{nucg} - \overline{u})$/N	−2.2	−0.3	1.0	−1.7	−0.4	0.5	−2.6	−0.8	0.5	−2.3	−1.7	−0.1
$(v_{nucg} - \overline{v})$/N	0.5	0.4	0.7	0.3	0.6	0.7	0.9	0.9	0.4	0.4	0.5	0.4
$(u_{nucg} - \overline{u})$/S	−2.9	−1.1	1.1	−1.7	−0.9	0.3	1.5	−1.2	0.7	−2.7	−1.8	−0.5
$(v_{nucg} - \overline{v})$/S	0.6	0.4	0.0	0.3	0.7	1.2	−1.0	0.9	0.3	0.2	0.4	0.9
$(u_{ucg} - u_{nucg})$/N	1.2	1.0	−0.2	1.4	0.7	−0.3	1.5	0.9	−0.1	0.5	0.3	0.0
$(v_{ucg} - v_{nucg})$/N	0.0	−0.1	−0.5	−0.4	−0.2	−0.5	−1.0	−1.0	−0.5	−0.6	−0.6	−0.9
$(u_{ucg} - u_{nucg})$/S	2.0	1.5	0.9	1.7	1.4	0.7	2.3	2.1	1.2	1.9	1.3	0.6
$(v_{ucg} - v_{nucg})$/S	0.2	0.2	0.5	−0.3	−0.3	0.4	−0.6	−0.6	0.5	−0.2	−0.1	−0.5

[a]$\overline{u}$: climatological mean of pre-summer u; $\overline{v}$: climatological mean of pre-summer v; u_{nucg}: mean u for CIs without UCGs; v_{nucg}: mean v for CIs without UCGs; u_{ucg}: mean u for CIs with UCGs; v_{ucg}: mean v for CIs with UCGs.

At 950 hPa, southerly anomalies are predominant at CSC for CIs without UCGs for both daytime and nocturnal sea-CIs (Figures 7k and 7l), as well as nocturnal land-CIs (Figure 7j). The distinction among these scenarios lies in that the southerly anomalies for nocturnal land-CIs tends to penetrate further inland to the north of CSC, whereas those for sea-CIs are confined to the sea surface of CSC. Additionally, daytime sea-CIs without UCGs exhibit a southwesterly anomaly, whereas nocturnal sea-CIs without UCGs displays a southeasterly anomaly. This difference is attributed to the diurnal variation of boundary-layer winds induced by inertia oscillation (Du et al., 2014, 2015). As summarized in Table 2, the maximum mean 950-hPa southerly anomaly of 1.2 m/s in the southern region of South China (the area south of 22°N as indicated in Figure 7a) is observed for the nocturnal land-CIs without UCGs, and the minimum of 0 m/s is observed for daytime land-CIs without UCGs. The 950-hPa southerly anomalies over the south of South China for sea-CIs fall in between these values, with 0.3 and 0.9 m/s for daytime and nocturnal sea-CIs without UCGs, respectively. The enhancement in 950-hPa southerly is anticipated to intensify the boundary-layer convergence and also the upward motions at CSC, creating favorable conditions for CIs. A westerly anomaly at 950 hPa is discernible over South China for daytime land-CIs without UCGs (Figure 7i), indicating that compared with the intensity of the meridional wind, the direction of the boundary-layer wind is more crucial for daytime land-CIs. Particularly, southwesterly boundary-layer winds are more conducive to daytime land-CIs, whereas the intensity of the meridional wind is consistent with the pre-summer mean.

The composite wind differences over South China between CIs with and without UCGs for various scenarios are presented in Figure 8. A 500-hPa westerly anomaly is discernible over CSC across all scenarios (Figures 8a–8d), compared to cases without UCGs. The centers of the westerly anomaly for land-CIs (Figures 8a and 8b) are located at the coast of South China, which is further norward in comparison to those for sea-CIs (Figures 8c and 8d). This westerly anomaly suggests an intensified 500-hPa westerly jet prevailing over CSC, thereby augmenting the divergence at 500 hPa in the region. It promotes upward motions from lower levels, consequently facilitates the upscale development of convective cells. The most pronounced westerly anomaly, exceeding 3 m/s, is observed for daytime sea-CIs with UCGs (Figure 8c).

A 700-hPa southwesterly anomaly is observed at CSC for daytime land-CIs with UCGs (Figure 8e), whereas a westerly anomaly characterizes the remaining scenarios (Figures 8f–8h). These westerly anomalies in 700 and 500-hPa winds likely account for the frequent northeastward moving of land-CIs (Figures 4a and 4c) and sea-CIs (Figures 4b and 4d) toward their upscale growths. In addition, a northeasterly anomaly situated in the northeast of South China is discernible across all scenarios. This spatial configuration of winds indicates a 700-hPa cyclonic

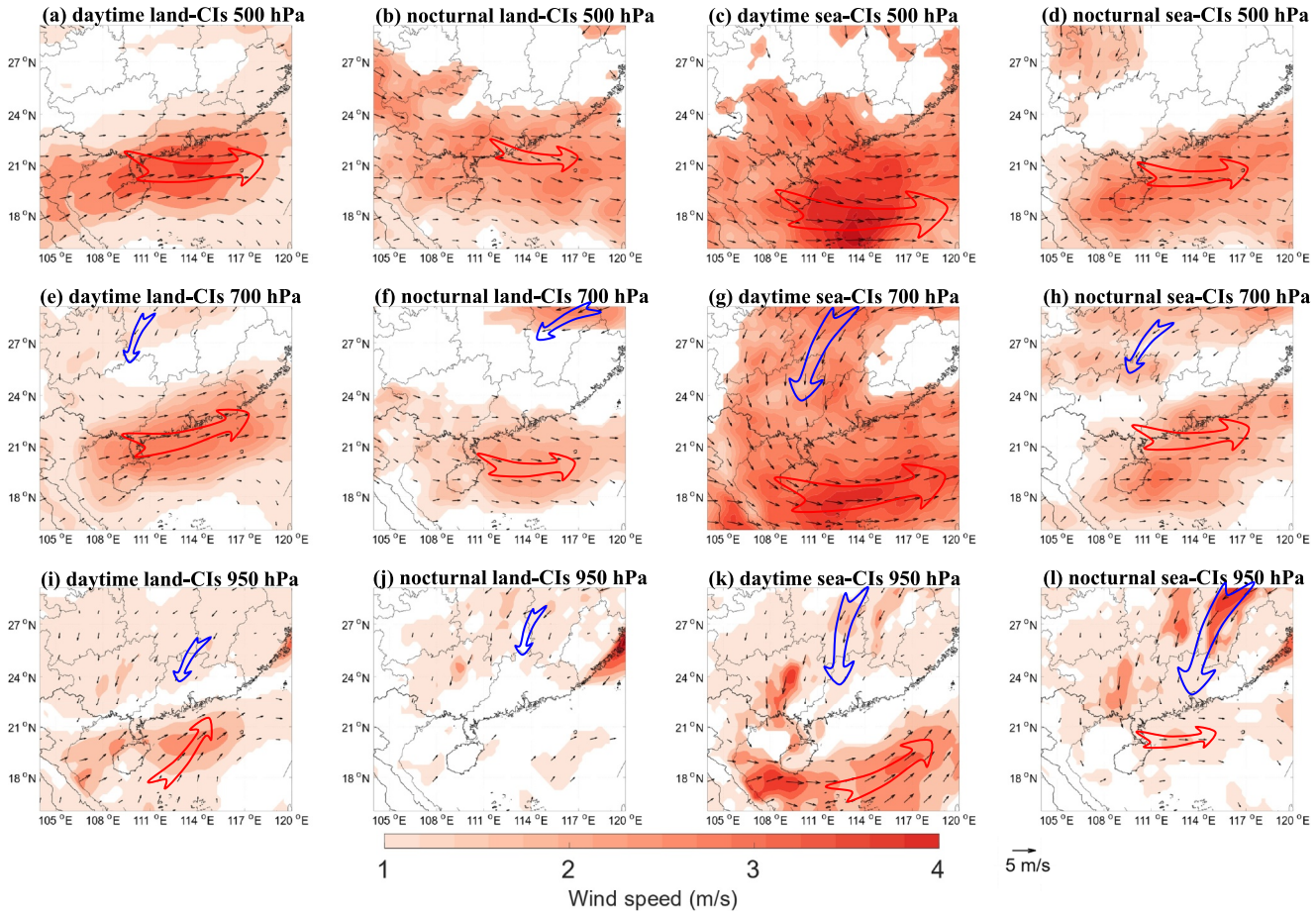

Figure 8. Composite wind differences between CIs with and without UCGs at 500-hPa (upper panel), 700-hPa (middle panel) and 950-hPa (lower panel) over South China for daytime land-CIs (a, e, and i), nocturnal land-CIs (b, f, and j), daytime sea-CIs (c, g, and k), and nocturnal sea-CIs (d, h, and l). Shaded colors indicate differences significant at the significance level of 0.01.

anomaly over South China for CIs with UCGs, suggesting upward motions in low levels crucial for convective cells to grow upscale. It is worth noting that the most pronounced 700-hPa westerly anomaly, exceeding 3 m/s, is also observed for daytime sea-CIs with UCGs (Figure 8g), with the center of anomaly located further southward compared to other scenarios.

As illustrated in Figures 8i–8k, compared with the CIs without UCGs, it exhibits a southwesterly anomaly at 950 hPa for CIs that grow upscale, except for the scenario of nocturnal sea-CIs. It suggests that enhanced boundary-layer southerly is closely related with CIs that grow upscale. A 950-hPa westerly anomaly is observed for nocturnal sea-CIs with UCGs (Figure 8l), indicating a shift of boundary-layer winds off the coast from southeasterly for nocturnal sea-CIs without UCGs (Figure 7l) to southwesterly for their counterparts that grow upscale. It suggests that the direction of the boundary-layer wind off the coast plays a greater role in facilitating the upscale growth of nocturnal sea-CIs than the intensity of the meridional wind. The most pronounced southwesterly anomaly at 950 hPa is identified for daytime sea-CIs with UCGs (Figure 8k), whereas relatively low southerly anomalies are observed for nocturnal land-CIs (Figure 8j) and nocturnal sea-CIs (Figure 8l) with UCGs. It is wrth noting that it exhibits a northeasterly anomaly extending from the northeast to the west coast of South China for CIs with UCGs, which forms a northeast-southwest horizontal wind shear at CSC with the southerly anomaly off the coast, promoting upward motions in the boundary layer over the region.

As summarized in Table 2, the most substantial westerly anomalies, reaching 2.3 m/s at 500 hPa and 2.1 m/s at 700 hPa, in conjunction with a southwesterly anomaly of 1.3 m/s at 950 hPa, are notably evident for daytime sea-CIs with UCGs. In contrast, nocturnal land-CIs and sea-CIs with UCGs shows relatively small anomalies in all layers.

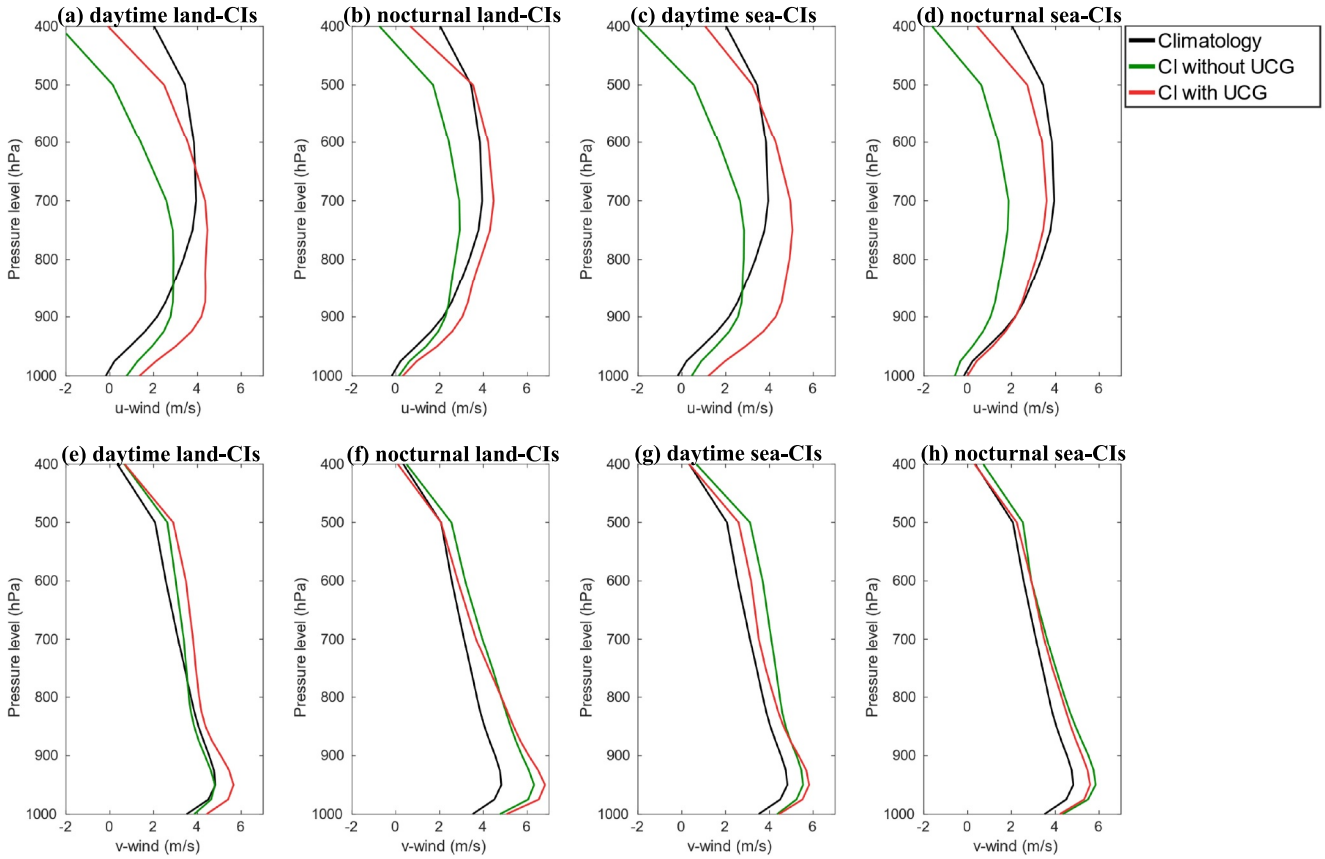

Figure 9. Composite vertical profiles for u- (upper panel) and v-component (lower panel) of horizontal winds averaged over coastal South China for daytime land-CIs (a, e), nocturnal land-CIs (b, f), daytime sea-CIs (c, g), and nocturnal sea-CIs (d, h).

4.1.2. Vertical Wind Shear

The composites of vertical profile for *u*- and *v*-winds over coastal South China for various CI-cases with and without UCGs are presented in Figure 9. For daytime land-CIs without UCGs, the *u*-wind manifests a slight westerly anomaly below 950 hPa, and an increasing easterly anomaly from 950 to 400 hPa compared to the pre-summer mean of 2013–2019 (Figure 9a); the *v*-wind is southerly in an equal magnitude with the pre-summer mean below 800 hPa (Figure 9e). For daytime land-CIs with UCGs, the *u*-wind demonstrates a significant westerly anomaly from the surface to 650 hPa compared to the pre-summer mean, with the maximum anomaly located at 900 hPa (Figure 9a); the *v*-wind exhibits a consistent southerly anomaly from the surface to 400 hPa, with the maximum anomaly located at 950 and 600 hPa (Figure 9e).

The composite *u*-wind profile for nocturnal land-CIs without UCGs aligns with the pre-summer mean below 900 hPa, whereas shows an increasing easterly anomaly from 900 to 400 hPa compared to the pre-summer mean (Figure 9b); the *v*-wind displays a significant southerly enhancement in from the surface to 400 hPa compared to the pre-summer mean, with the maximum enhancement observed within the boundary layer (Figure 9f). For nocturnal land-CIs with UCGs, the *u*-wind reveals a westerly anomaly from the surface to 500 hPa relative to the pre-summer mean (Figure 9b); the *v*-wind exhibits a southerly enhancement from the surface to 500 hPa compared to the pre-summer mean, with the enhancement slightly exceeding that observed for nocturnal land-CIs without UCGs within the boundary layer (Figure 9f).

For daytime sea-CIs without UCGs, the *u*-wind shows a slight westerly anomaly below 850 hPa, and a marked easterly anomaly from 950 to 400 hPa compared to the pre-summer mean (Figure 9c); the *v*-wind displays a consistent southerly anomaly from the surface to 400 hPa relative to the pre-summer mean (Figure 9g). For daytime sea-CIs with UCGs, the *u*-wind demonstrates a substantial westerly anomaly from the surface to 500 hPa compared to the pre-summer mean, with the maximum anomaly located at 900 hPa (Figure 9c); the *v*-wind

showcases a similar anomaly as the case for daytime sea-CIs without UCGs, only with a smaller magnitude for the anomaly above 900 hPa (Figure 9g).

For nocturnal sea-CIs without UCGs, the *u*-wind exhibits an increasing easterly anomaly from the surface to 400 hPa (Figure 9d), and the *v*-wind showcases a southerly anomaly from the surface to 400 hPa, with the maximum southerly anomaly observed at 950 hPa (Figure 9h), compared to the pre-summer mean. For nocturnal sea-CIs with UCGs, the *u*-wind demonstrates a profile approximately identical with the pre-summer mean (Figure 9d); the *v*-wind exhibits a southerly anomaly consistent with the pattern observed for nocturnal sea-CIs without UCGs (Figure 9h).

Overall, CIs without UCGs demonstrate a southerly anomaly particularly within the boundary layer, and an easterly anomaly above 850 hPa compared to the pre-summer mean for all scenarios, except daytime land-Cis. This indicates a counterclockwise vertical wind shear from the surface to mid-atmosphere over CSC. Conversely, CIs with UCGs demonstrate slight southerly anomaly within the boundary layer, yet a pronounced westerly anomaly in low levels from 900 to 700 hPa relative to their counterparts without UCGs, indicating a clockwise vertical wind shear from the surface to mid-atmosphere over CSC. These patterns of vertical wind shear further demonstrate that CIs are closely associated with favorable dynamic conditions (southerly anomaly relative to pre-summer mean) within the boundary layer in CSC, with the exception of daytime land-CIs. The boundary-layer uplifting force is provided by daytime solar heating over land area (Figure 9e). Conversely, low-level winds, particularly *u*-wind, over CSC, which is associated with the southern branch of the low-level anticyclonic anomaly over South China observed in Figure 7 or the cyclonic anomaly in Figure 8, play a pivotal role in determining whether a convective cell grows upscale or dissipates.

4.1.3. Vertical Velocity

The composite anomalies of vertical velocity at 500, 700 and 950-hPa over South China for various CI-cases without UCGs relative to the pre-summer mean are presented in Figure 10. Upon comparing with the pre-summer mean, the boundary-layer vertical velocity for daytime land-CIs without UCGs manifests an overall upward anomaly at 950 hPa over land area of CSC (Figure 10i). This is likely a consequence of the daytime solar heating, given the absence of enhancement in boundary-layer southerlies for daytime land-CIs without UCGs (Figure 7i). It is worth noting that a significant downward anomaly within the boundary layer is evident over the sea surface of CSC for daytime land-CIs without UCGs. This is associated with the reinforcement of the land-sea breeze circulation at CSC due to the intensified solar heating over land, which further demonstrates that the enhancement in the boundary-layer upward motion over land for daytime land-CIs is attributed to favorable thermal conditions. However, the vertical velocity at 500 (Figures 10a) and 700 hPa (Figure 10e) over CSC generally exhibits a downward anomaly for daytime land-CIs without UCGs. This deep downward anomaly is promoted by the 500-hPa easterly anomaly (Figures 7a) and 700-hPa anticyclonic anomaly (Figure 7e) over CSC. The diminished mid-level divergence induced by the 500-hPa easterly anomaly, combining with the enhancement in low-level convergence resulted from the 700-hPa anticyclonic anomaly, leading to large-scale downward motions in low- and mid-atmosphere at CSC.

For nocturnal land-CIs without UCGs, the composite vertical velocity demonstrates a significant upward anomaly within the boundary layer off the coast of CSC (Figure 10j), which is attributed to the enhanced boundary-layer southerlies for this scenario (Figure 7j) compared to the pre-summer mean. This upward anomaly corresponds to the occurrences of the nocturnal land-CIs at CSC. However, the vertical velocity at 700 (Figures 10f) and 500 hPa (Figure 10b) exhibits a prevailing downward anomaly over the land area of CSC, except over the region to the west of 110°E. This downward anomaly is associated with the low-level anticyclonic anomaly (Figure 7f) and the mid-level easterly anomaly (Figure 7b) over CSC. Meanwhile, the easterly anomalies at 500 hPa and the south branch of the 700-hPa anticyclonic anomaly and at CSC results in low- and mid-level convergence to the west of CSC, leading to upward anomalies at these levels over the region. This environment suppresses the development of convective cells in CSC, but is conducive for the UCG in the region to the west of CSC.

For daytime sea-CIs without UCGs, the composite vertical velocity manifests a significant upward anomaly within the boundary layer over the sea surface of CSC (Figure 10k), which is induced by the boundary-layer southerly anomaly for the scenario (Figure 7k). This upward anomaly is further off the coast of CSC compared to the case for nocturnal land-CIs without UCGs, aligning with the locations of the daytime sea-CIs. However, similar to the case for nocturnal land-CIs without UCGs, the vertical velocity at 700 (Figures 10g) and

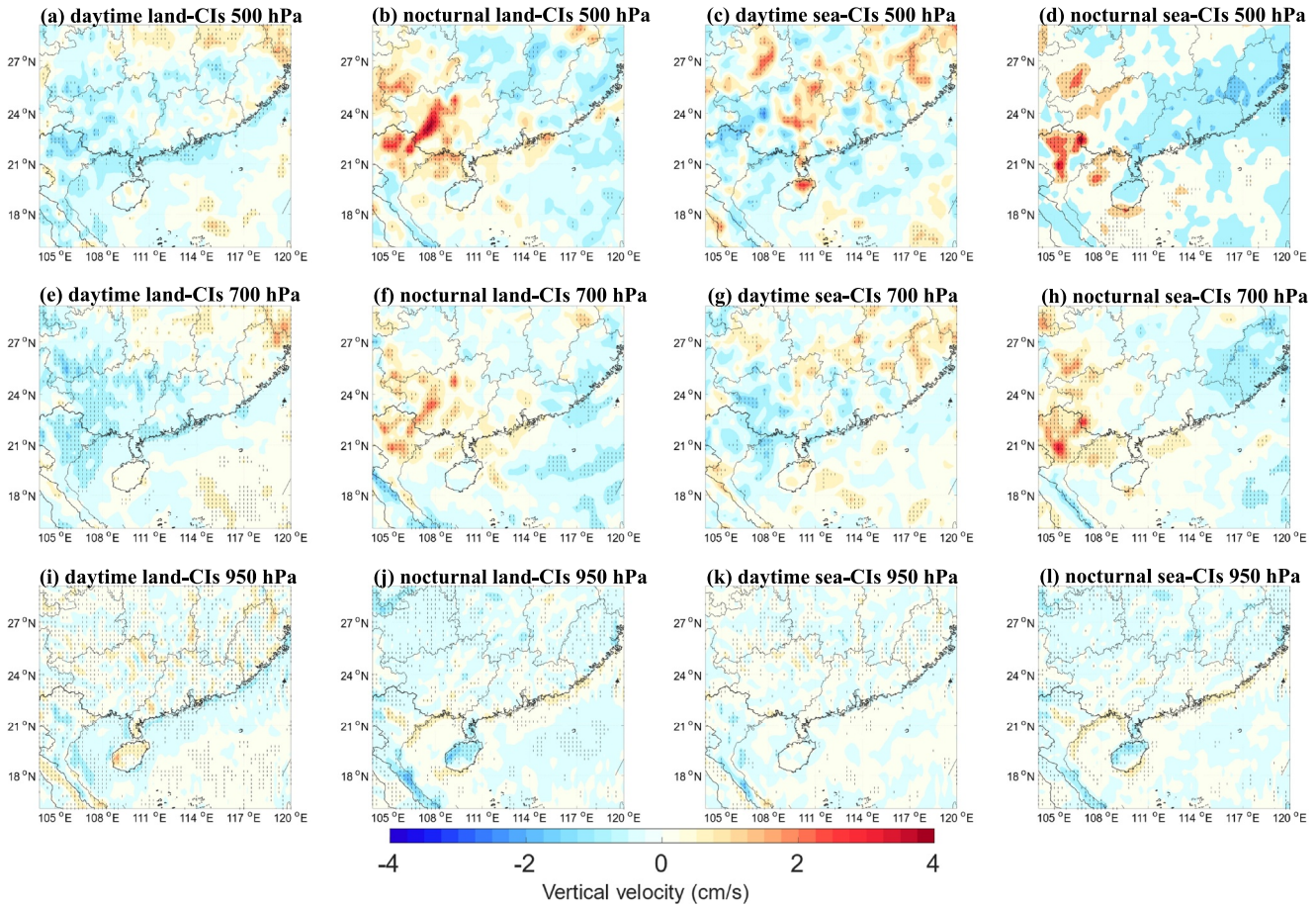

Figure 10. Composite differences in vertical velocity between CIs without UCGs and pre-summer mean at 500-hPa (upper panel), 700-hPa (middle panel) and 950-hPa (lower panel) over South China for daytime land-CIs (a, e, and i), nocturnal land-CIs (b, f, and j), daytime sea-CIs (c, g, and k), and nocturnal sea-CIs (d, h, and l). Shaded colors indicate positive anomalies in vertical velocity for CIs with UCGs relative to CIs without UCGs, and dash lines indicate differences significant at the significance level of 0.01.

500 hPa (Figure 10c) demonstrates a prevailing downward anomaly over CSC due to low-level anticyclonic anomaly (Figure 7g) and the mid-level easterly anomaly (Figure 7c) over CSC, suppressing the further development of convective cells in the region.

The composite vertical velocity for nocturnal sea-CIs without UCGs exhibits similar patterns of anomalies to the case of nocturnal land-CIs without UCGs at all three levels. A notable upward anomaly is observed at 950 hPa along the coast of CSC (Figure 10l), which is due to the enhanced boundary-layer southerly over the sea surface off the coast of CSC (Figure 7l). Despite the similarities in boundary-layer vertical velocity anomalies for both nocturnal land-CIs and nocturnal sea-CIs without UCGs, the locations of CIs for these two scenarios are different. This is likely attributed to the direction of the boundary-layer wind anomaly. Specifically, a southwesterly anomaly at the boundary layer (Figure 7j) is associated with land-CIs, whereas a southerly anomaly at the boundary layer (Figure 7l) may indicate sea-CIs. The vertical velocity at 700 (Figures 10h) and 500 hPa (Figure 10d) reveal a prevailing downward anomaly over the land area of CSC, except over the region to the west of CSC, which aligns with the case of nocturnal land-CIs without UCGs, and leads to an environment hampering the development of convective cells in CSC.

The composite anomalies of vertical velocity at 500, 700 and 950-hPa over South China for various CI-cases with UCGs relative to their counterparts without UCGs are illustrated in Figure 11. For daytime land-CIs with UCGs, the boundary-layer vertical velocity reveals a significant upward anomaly off the coast of CSC (Figure 11i), corresponding to the boundary-layer wind shear induced by the enhanced boundary-layer southwesterly anomaly off the coast of CSC and the northeasterly anomaly to the north of CSC (Figure 8i) compared to daytime land-CIs

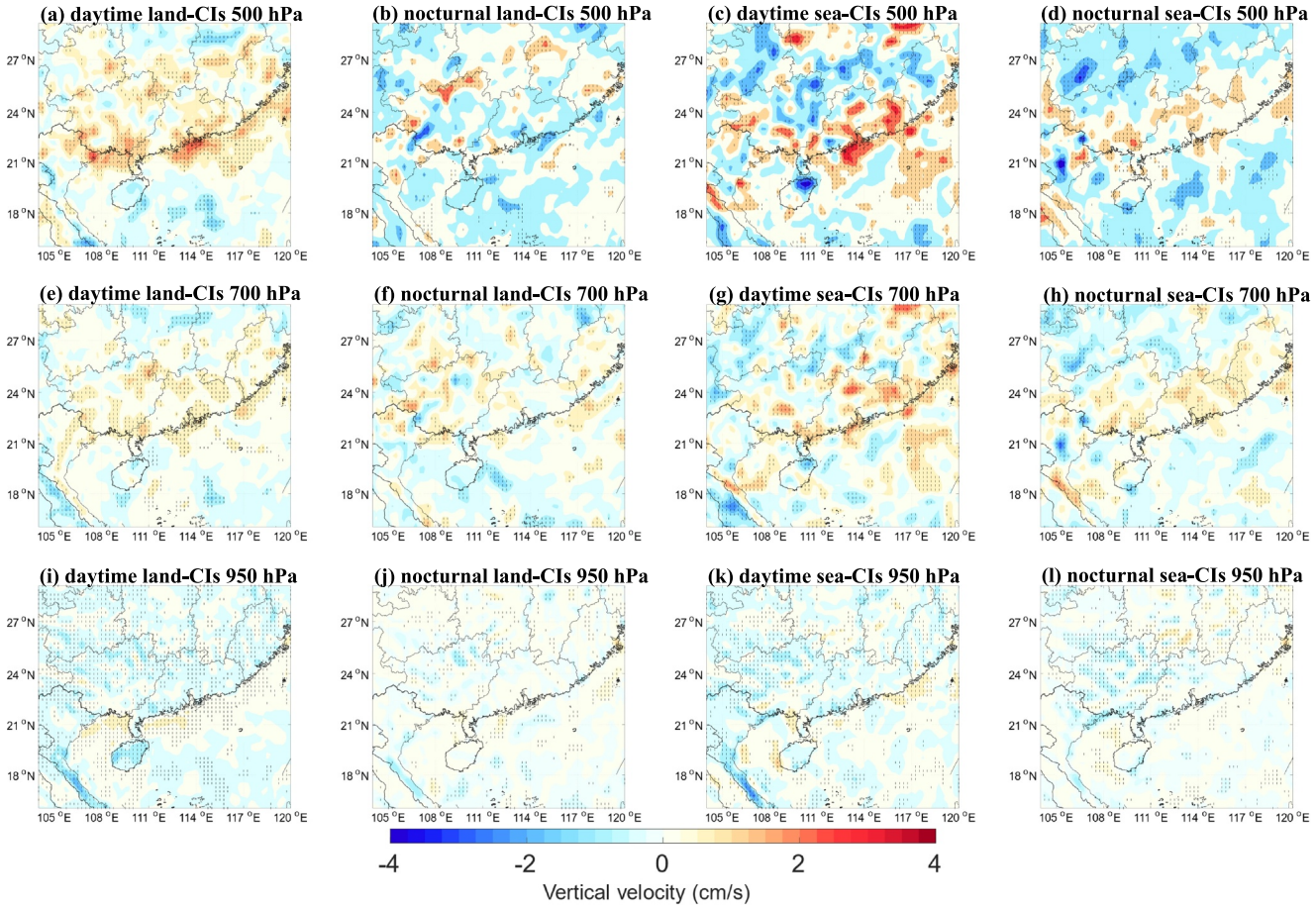

Figure 11. Composite differences in vertical velocity between CIs with and without UCGs at 500-hPa (upper panel), 700-hPa (middle panel) and 950-hPa (lower panel) over South China for daytime land-CIs (a, e, and i), nocturnal land-CIs (b, f, and j), daytime sea-CIs (c, g, and k), and nocturnal sea-CIs (d, h, and l). Shaded colors indicate positive anomalies in vertical velocity for CIs with UCGs relative to CIs without UCGs, and dash lines indicate differences significant at the significance level of 0.01.

without UCGs. Additionally, the 700- (Figures 11e) and 500-hPa (Figure 11a) vertical velocity for daytime land-CIs with UCGs exhibits a pronounced upward anomaly across the entire CSC, which is attributed to the 700-hPa cyclonic anomaly (Figure 8e) and the 500-hPa westerly anomaly (Figure 8a) observed for this scenario. The vertical velocity anomalies demonstrate a large-scale deep upward motion from the boundary layer to mid-atmosphere over CSC, which is conducive for the development of convective cells in the region.

For nocturnal land-CIs with UCGs, the boundary-layer vertical velocity depicts a general upward anomaly across CSC compared to their counterparts without UCGs, with the most pronounced upward anomaly located near the coast (Figure 11j). The 700-hPa vertical velocity also displays an upward anomaly (Figure 11f), whereas the 500-hPa vertical velocity exhibits no significant anomaly over CSC (Figure 11b), indicating that the upward anomaly for this scenario is not as pronounced and deep and that observed for daytime land-CIs with UCGs. This pattern corresponds to the weaker rainfall induced by nocturnal land-CIs with UCGs (Figure 6d) in comparison to daytime land-CIs with UCGs (Figure 6b).

The vertical velocity anomalies observed for daytime sea-CIs with UCGs relative to their counterparts without UCGs are similar to those for daytime land-CIs with UCGs at all three levels, but with a smaller magnitude in the boundary layer (Figure 11k), and significantly larger magnitudes at 700 (Figures 11g) and 500 hPa (Figure 11c). These patterns of the vertical velocity anomalies indicate the most pronounced and deep large-scale upward motion associated with daytime sea-CIs with UCGs, corresponding to the most intensified rainfall observed for this scenario among all scenarios (Figure 6f).

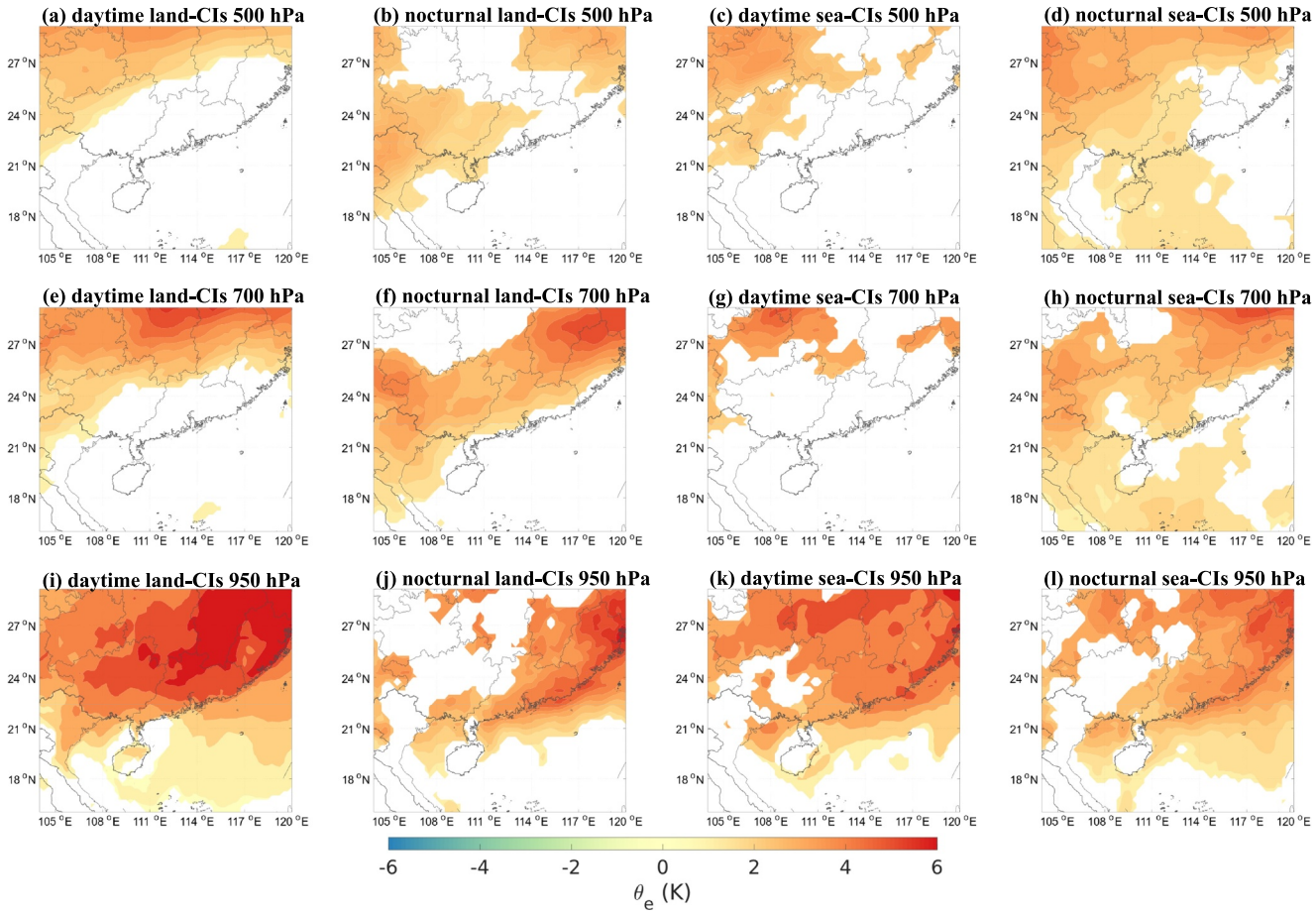

Figure 12. Composite θ_e differences between CIs without UCGs and pre-summer mean at 500-hPa (upper panel), 700-hPa (middle panel) and 950-hPa (lower panel) over South China for daytime land-CIs (a, e, and i), nocturnal land-CIs (b, f, and j), daytime sea-CIs (c, g, and k), and nocturnal sea-CIs (d, h, and l). Shaded colors indicate differences significant at the significance level of 0.01.

For nocturnal sea-CIs with UCGs, the boundary-layer vertical velocity exhibits a weak upward anomaly off the coast of CSC compared to their counterparts without UCGs (Figure 11l). The 700- (Figures 11h) and 500-hPa (Figure 11d) vertical velocity also demonstrates an upward anomaly over CSC, which is similar to the cases for daytime land-CIs (Figures 11a and 11e) and daytime sea-CIs with UCGs (Figures 11c and 11g), albeit with smaller magnitudes relative to these two scenarios. This less pronounced upward motion aligns with the relatively weak rainfall over CSC induced by nocturnal sea-CIs with UCGs (Figure 6h).

The analysis in this section demonstrates that pre-summer CIs at CSC are closely related with enhanced boundary-layer southerly off the coast of CSC and northerly to the north of CSC, which produces a boundary-layer wind shear and convergence at CSC. Additionally, it is worth noting that slight difference in the boundary-layer wind fields could lead to different locations of CIs, which consequently affects the locations of the MCSs evolved from these convective cells, and thus the region of rainfall induced by MCSs. On the contrary, the anticyclonic anomaly at 700 hPa and easterly anomaly at 500 hPa over South China associated with CIs without UCGs imply that the unfavorable dynamic conditions at the low- to mid-levels are the primary obstacles to the upscale growth of convective cells. It suggests that both boundary-layer and low-level convergence, along with mid-level divergence, are equally crucial for the UCG. Convergence at lower levels, coupled with divergence at mid-level, creates a large-scale deep vertical motion that continuously transports warm and moist air from the surface to mid-troposphere or above, facilitating the upscale development of convective cells.

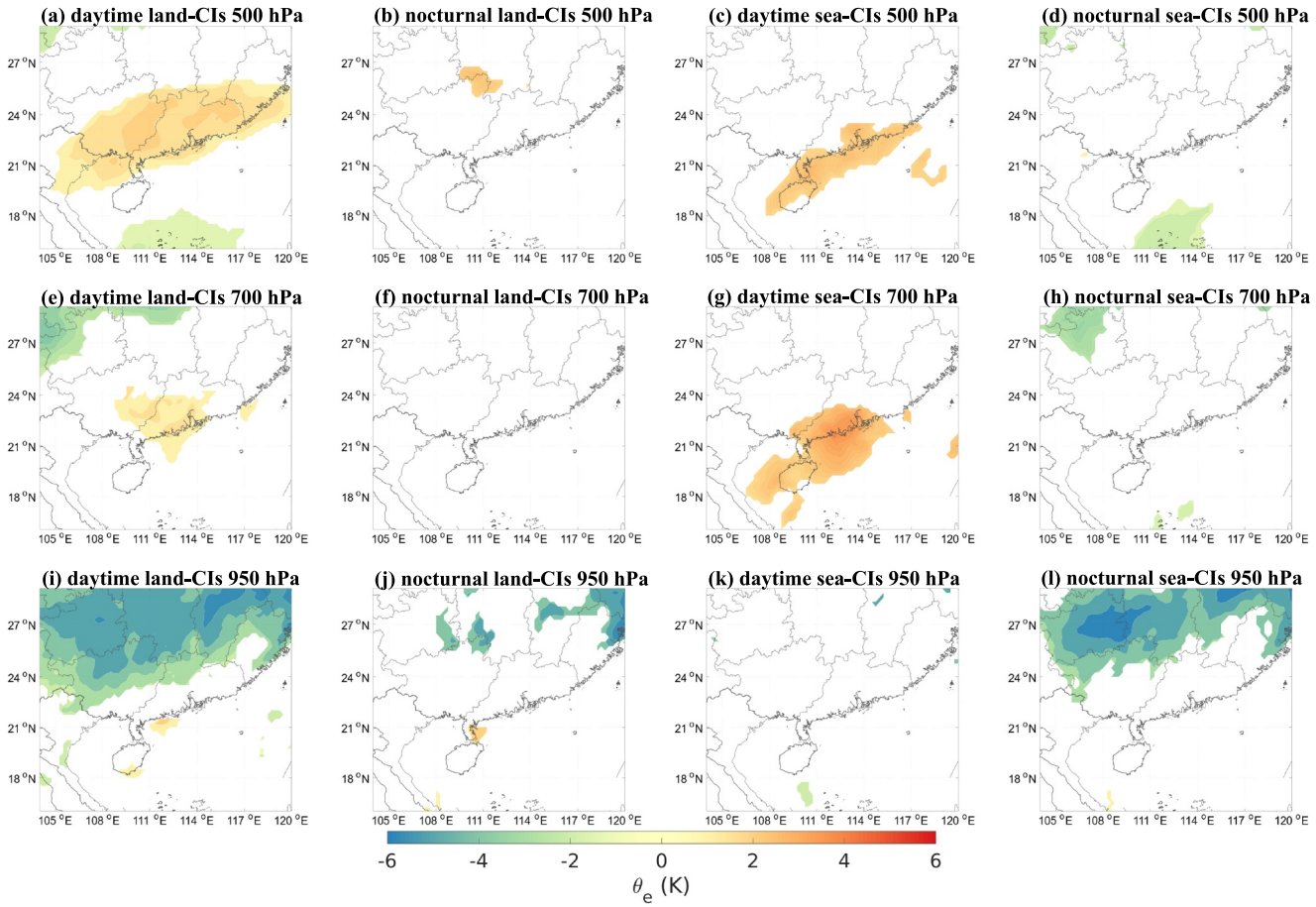

Figure 13. Composite θ_e differences between CIs with and without UCGs at 500-hPa (upper panel), 700-hPa (middle panel) and 950-hPa (lower panel) over South China for daytime land-CIs (a, e, and i), nocturnal land-CIs (b, f, and j), daytime sea-CIs (c, g, and k), and nocturnal sea-CIs (d, h, and l) without UCGs. Shaded colors indicate differences significant at the significance level of 0.01.

4.2. Thermodynamics

Figure 12 presents the composite differences of equivalent potential temperature (θ_e) over South China between CIs without UCGs and pre-summer mean. Similar distributions of θ_e anomalies are observed for all scenarios at each layer, despite disparities in the magnitude of these anomalies. Relative to the pre-summer mean, an increase in θ_e over land area to the north of South China is observed at 500 (Figures 12a and 12c) and 700 hPa (Figures 12e and 12g) for daytime CIs without UCGs, irrespective of whether they initiate on or off the coast. By contrary, the enhancement in θ_e at 500 and 700 hPa is located further southward over South China for nocturnal CIs without UCGs (Figures 12b–12d, 12f, and 12h). The most pronounced increase in θ_e is observed at 950 hPa (Figures 12i and 12k) across the entire South China for CIs without UCGs, particularly for daytime land-CIs without UCGs (Figure 12i). These patterns suggest a close relationship between the CIs at CSC and low-level thermodynamic conditions.

The composite θ_e differences between CIs with and without UCGs for various scenarios are illustrated in Figure 13. Significant enhancements in 700- and 500-hPa θ_e are notably discernible for daytime land- (Figures 13a and 13e) and sea-CIs (Figures 13c and 13g) with UCGs, particularly the latter, with the maximum θ_e anomaly exceeding 1.5 K at both levels. Nocturnal land-CIs with UCGs shows moderate θ_e enhancements at 700 and 500 hPa over the region further northward compared to other scenarios. These patterns suggest an enhancement in the deep vertical transport of warm and moist air from low to mid atmosphere, fostering the upscale growths of convective cells. In contrast, no significant θ_e enhancements at 700- and 500-hPa are discerned for nocturnal and sea-CIs (Figures 13d and 13h) with UCGs.

Compared with the CIs without UCGs, an augmentation in 950-hPa θ_e is identified at the coast of South China for land-CIs with UCGs (Figures 13i and 13j). A greater enhancement is observed for nocturnal land-CIs with UCGs. Figure 13j illustrates a significant increase in 950-hPa θ_e exceeding 1.5 K at the west coast of South China for nocturnal land-CIs with UCGs. By contrary, the region with enhanced 950-hPa θ_e become considerably reduced for daytime land-CIs with UCGs (Figure 13i). Conversely, no significant enhancement in 950-hPa θ_e is found for sea-CIs with UCGs (Figures 13k and 13l), particularly for nocturnal sea-CIs with UCGs (Figure 13l), implying that an enhancement in 950-hPa θ_e may not be a prerequisite for the upscale development of sea-CIs. It is worth noting that it exhibits a remarked decrease in 950-hPa θ_e over the land area of South China for the CIs that grow upscale, compared to the CIs without UCGs. This decrease in 950-hPa θ_e, with the maximum anomaly exceeding −3 K, becomes more pronounced from the coast toward the inland areas in the north. The most significant decrease in 950-hPa θ_e is observed for daytime land-CIs (Figure 13i) and nocturnal sea-CIs (Figure 13l) with UCGs. By contrary, nocturnal land-CIs (Figure 13j) and daytime sea-CIs (Figure 13k) exhibit relatively minor negative anomalies in 950-hPa θ_e for CIs that develop.

The spatial patterns of θ_e differences between CIs with and without UCGs are the results of the corresponding anomalies in wind fields associated with large-scale synoptic conditions. The decrease in 950-hPa θ_e over the land area of South China is attributed to the southwestward transport of dry and cold air by the northeasterly anomalies in the northeast of South China. The most pronounced northeasterly anomalies (Figures 8i and 8k) results in the most substantial decrease in 950-hPa θ_e (Figures 13i and 13k) in the region, which is observed for daytime land-CIs and sea-CIs with UCGs. The cyclonic anomalies in the 700-hPa wind field for CIs with UCGs promotes the upward motions over the land areas of South China (Figures 8e–8h), leading to enhanced 700-hPa (Figures 13e–13h) and 500-hPa θ_e (Figures 13a–13d) in the region, with the greatest enhancement observed for daytime sea-CIs with UCGs (Figures 13c and 13g), and the smallest enhancement for nocturnal sea-CIs with UCGs (Figures 13d and 13h). In general, the increase in θ_e in the low-to mid-atmosphere provides a conducive thermodynamic environment for the development of CIs with UCGs, particularly for daytime CIs with UCGs.

4.3. Atmospheric Instability

The anomalies in thermodynamic conditions associated with CIs with and without UCGs results in the different patterns for the convective available potential energy (CAPE). Compared with the pre-summer mean, the CAPE for CIs without UCGs shows a general enhancement in CSC. However, the enhancement in CAPE is located at the landside of the CSC for daytime CIs (Figures 14a and 14e), whereas mainly over the sea surface of the CSC for nocturnal CIs (Figures 14c and 14g). The most pronounced enhancement in CAPE is observed for nocturnal land-CIs (Figure 14c), indicating a heightened necessity for enhanced atmospheric instability to facilitate nocturnal land-CIs. By contrary, it shows considerably lower requirements for atmospheric instability to trigger sea-CIs (Figures 14e and 14g), particularly for nocturnal sea-CIs (Figure 14g). This is likely attributed to the greater humidity over the sea surface, providing a conducive moist environment for the occurrence of moisture convections.

Compared to CIs without UCGs, the CAPE for CIs with UCGs shows an enhancement predominantly confined to the north of the South China Sea. The most pronounced enhancement in CAPE over the sea surface is observed for daytime land-CIs (Figure 14b), indicating the utmost requirement for enhanced atmospheric instability to facilitate the upscale growth of daytime land-CIs. The situations observed for nocturnal land-CIs (Figure 14d) and nocturnal sea-CIs (Figure 14h) with UCGs are similar to that for daytime land-CIs, albeit with smaller magnitudes in the anomalies. Meanwhile, relative to their counterparts without UCGs, a decrease in CAPE over the land area of South China is observed for all CIs with UCGs (Figures 14b–14d, 14f, and 14h), suggesting a significant low-level thermal contrast at CSC for CIs with UCGs. This is due to the boundary-layer and low-level northeasterly anomaly to the north of CSC (Figure 8), which transports low-θ_e air masses to CSC. The most pronounced decrease in CAPE over land area is observed for daytime land-CIs with UCGs (Figure 14b). This is attributed to the relatively high-CAPE environment over land area for daytime land-CIs (Figures 12i and 14a), which is particularly sensitive to the low-θ_e air masses from the north compared with the other three scenarios.

5. Conclusions and Discussion

Characteristics of pre-summer UCGs at CSC exhibit pronounced diurnal and land-sea disparities. Specifically, land-CIs tend to grow upscale during the daytime, whereas sea-CIs are more likely to develop at night. About 75%

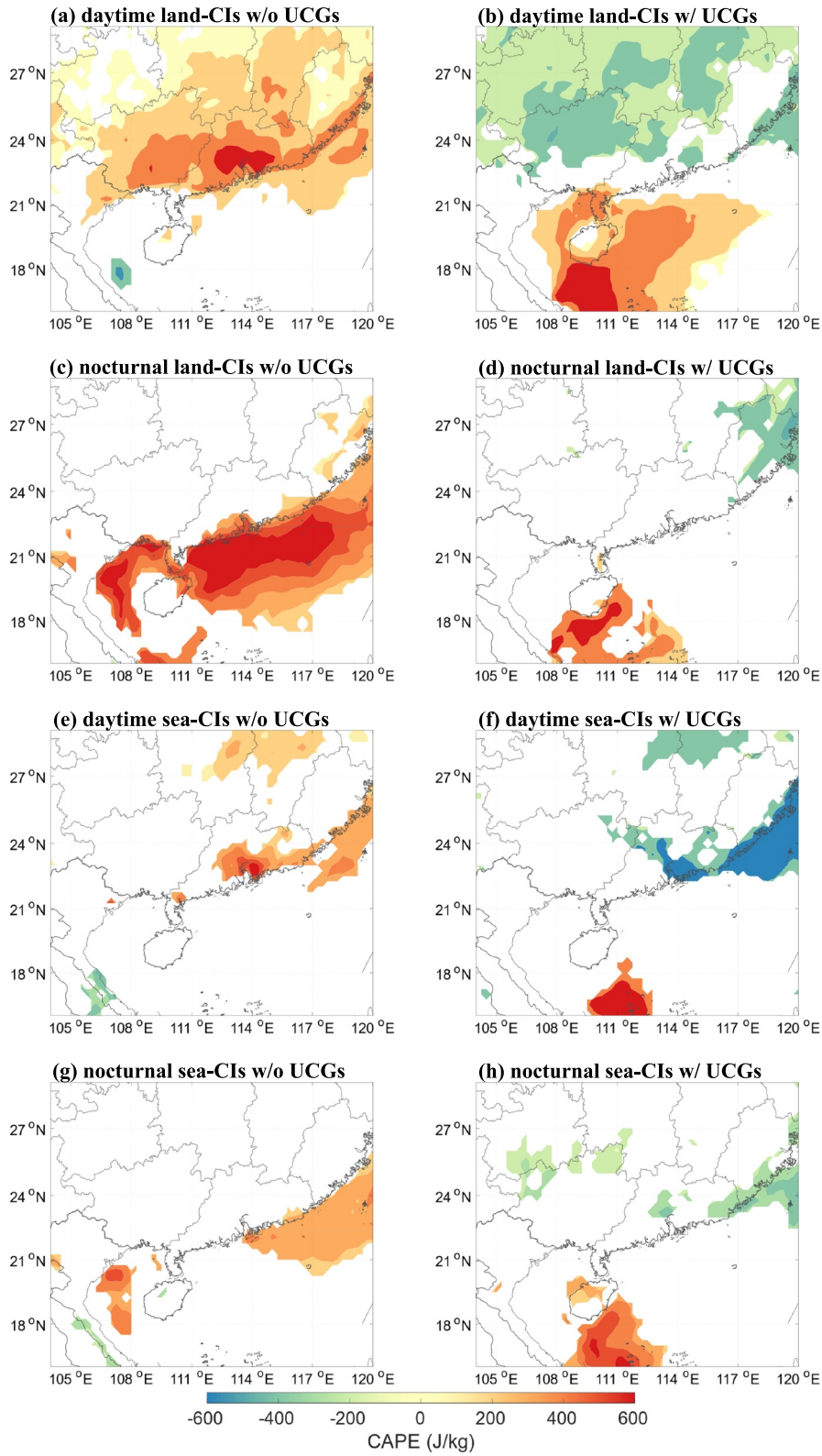

Figure 14. Composite differences of convective available potential energy (CAPE) over South China between CIs without UCGs and pre-summer mean (left panel), and between CIs with and without UCGs (right panel) for daytime land-CIs (a–b), nocturnal land-CIs (c–d), daytime sea-CIs (e–f), and nocturnal sea-CIs (g–h). The shaded colors indicate differences significant at the significance level of 0.01.

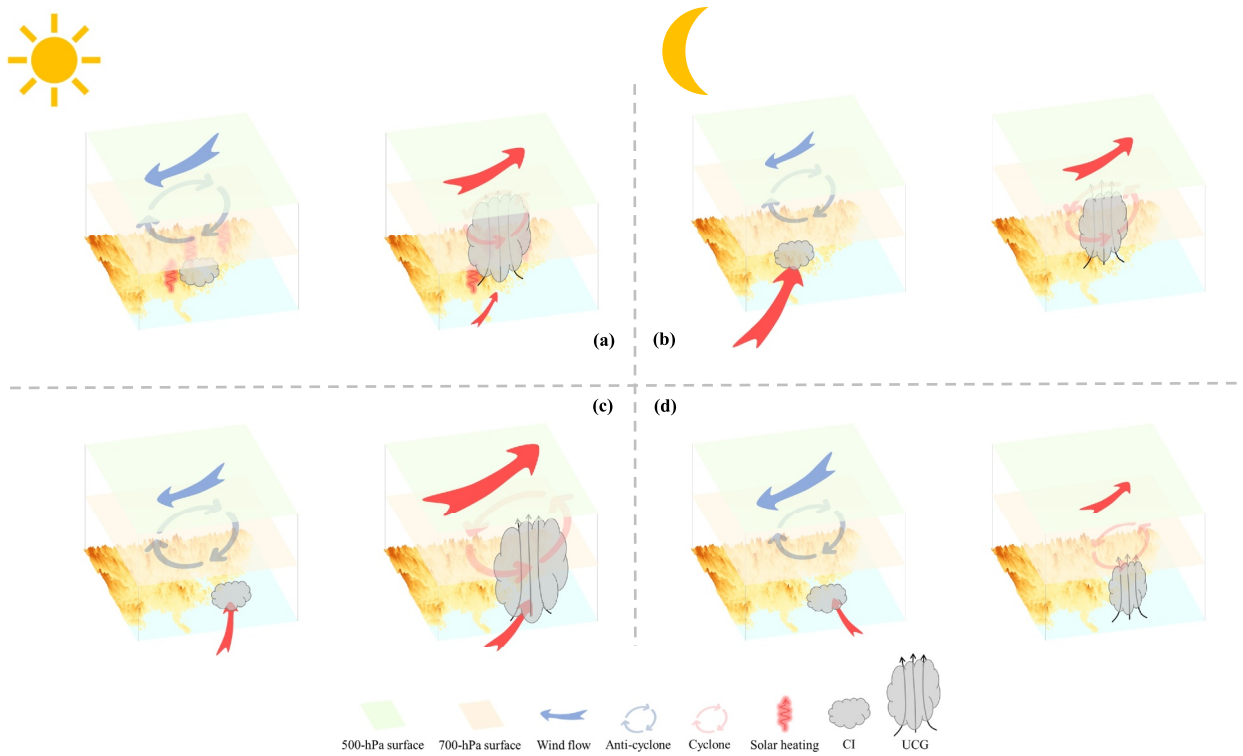

Figure 15. Conceptual illustration for the UCGs of daytime land-CIs (a), nocturnal land-CIs (b), daytime sea-CIs (c), and nocturnal sea-CIs (d).

of land-CIs with UCGs occur during the daytime, peaking in the afternoon, whereas approximately 64% of sea-CIs with UCGs occur at night, peaking in the early morning. Nocturnal sea-CIs have the highest likelihood (53%) of developing upscale to MCSs, compared to around 40% or lower for other scenarios.

Pre-summer CIs at CSC are primarily driven by the intensity of the boundary-layer convergence in the region, with limited dependence on conditions above the boundary layer. However, UCGs result from enhanced dynamic and thermodynamic environments spanning from the surface to the mid-troposphere or higher layers, compared to CIs without UCGs. Enhanced boundary-layer southerly winds off the coast and northeasterly anomalies to the north of South China contribute to augmented near-surface moisture convergence in CSC. Convergence at lower levels, along with divergence at mid-levels, creates an upward channel that facilitates the transport of warm and moist air from the surface to the mid-troposphere. The enhanced moisture uplifted to higher levels results in a greater release of latent heat, thereby promoting UCGs. This study highlights the dominant role of environmental dynamic conditions in promoting the UCG of convective cells at CSC. The key environmental factors include low-level jet, low-level vortex/shearline, mid-level westerly jet, and vertical wind shear, which are consistent with the findings of previous studies on UCGs in different regions (Coniglio et al., 2011; Du, Chen, Han, Mai et al., 2020; French & Parker, 2010; Shen et al., 2020). These factors are considered to be important to UCGs in other regions, such as Central United States (Coniglio et al., 2011), and central and northern Argentina (Zhang et al., 2021). The favorable environmental thermodynamic conditions including greater equivalent potential temperature and convective available potential energy, which resulted from the above-mentioned anomalies in wind fields, are another crucial reason for convective development at CSC, particularly for daytime convective cells initiated over land. The relatively minor role of the thermodynamic conditions compared to dynamic factors in promoting UCGs at CSC is likely due to the location of the region. Being a subtropical coastal region significantly affected by the East Asian Summer Monsoon during warm season, CSC is characterized by abundant available heat and moisture.

The conceptual model illustrating the large-scale environment for CIs with and without UCGs in different scenarios are demonstrated in Figure 15. During the daytime, the atmospheric instability and extra upward lifting force provided by solar heating over land makes land-CIs more likely to occur even under weak dynamic conditions that suppress UCGs (Figure 15a). This indicates that a greater enhancement in the boundary-layer

southerly, as well as low-to mid-level westerly, are required for overcoming the unfavorable dynamic environment and promote the upscale growth of convective cells initiated over land during daytime (Figure 15a). On the other hand, the land-sea thermal contrast at CSC leads to enhanced downward motion in the boundary layer over sea surface during the daytime, making daytime sea-CIs less likely to occur and even harder to develop (Figure 15c). Under such circumstances, extremely strong boundary-layer and low-level convergence, along with mid-level divergence, are required to facilitate UCGs of sea-CIs (Figure 15c). This results in the most pronounced large-scale upward motion, as well as the most intensive convection and rainfall for daytime sea-CIs with UCGs among all scenarios.

At night, decreased near-surface temperature indicates that a higher dynamic threshold, that is, stronger boundary-layer southerly winds and low- and mid-level westerly winds, is required at CSC to provide sufficient uplifting force for nocturnal CIs to occur (Figure 15b). However, once convection is triggered, a smaller enhancement in dynamic conditions is needed for nocturnal CIs to grow upscale. Furthermore, a greater enhancement in boundary-layer thermal and moisture conditions is required for nocturnal land-CIs (Figure 15b) to upscale compared to sea-CIs. This is due to the lower near-surface temperature and moisture over land during the nighttime, which promotes low-level atmospheric stability, making nocturnal UCGs less likely to occur over land. In contrast, the higher near-surface temperature over sea surface during the nighttime results in enhanced atmospheric instability and upward motion in the boundary layer, which are preferable for CIs over sea surface (Figure 15d). These favorable dynamic conditions, coupled with the abundant moisture over the sea surface, make nocturnal sea-CIs the most likely to upscale among all scenarios. This explains the highest probability and the lowest requirements for dynamic and thermodynamic conditions for nocturnal sea-CIs to upscale (Figure 15d). Meanwhile, Lower requirements for dynamic and thermodynamic conditions for nocturnal sea-CIs to upscale also indicate relatively low intensity of UCGs, leading to the lightest rainfall produced by sea-CIs with UCGs among all scenarios.

Data Availability Statement

The data for convection initiation and upscale convective growth at coastal South China are available at Su (2024).

Acknowledgments
This work was supported by the National Natural Science Foundation of China (Grants U2242203, 42122033, 42275006, and 4240050041), the Natural Science Foundation of Guangdong, China (Grants 2022A1515110925, and 2024A1515012571), and the Key Innovation Team of China Meteorological Administration (CMA2023ZD08), Supported by Southern Marine Science and Engineering Guangdong Laboratory (Zhuhai) (SML2024SP035).

References

Bai, L., Chen, G., & Huang, L. (2020a). Convection initiation in monsoon coastal areas (South China). *Geophysical Research Letters*, *47*(11), e2020GL087035. https://doi.org/10.1029/2020gl087035

Bai, L., Chen, G., & Huang, L. (2020b). Image processing of radar mosaics for the climatology of convection initiation in South China. *Journal of Applied Meteorology and Climatology*, *59*(1), 65–81. https://doi.org/10.1175/jamc-d-19-0081.1

Bai, L., Chen, G., Huang, Y., & Meng, Z. (2021). Convection initiation at a coastal rainfall hotspot in South China: Synoptic patterns and orographic effects. *Journal of Geophysical Research: Atmospheres*, *126*(24), e2021JD034642. https://doi.org/10.1029/2021jd034642

Bao, X., Luo, Y., & Gao, X. (2021). The synoptic impacts on the convection initiation of a warm-sector heavy rainfall event over coastal South China prior to the monsoon onset: A numerical modeling study. *Journal of Geophysical Research: Atmospheres*, *126*(14), e2020JD034335. https://doi.org/10.1029/2020jd034335

Chao, L., Huang, B., Yuanjian, Y., Jones, P., Cheng, J., Yang, Y., & Li, Q. (2020). A new evaluation of the role of urbanization to warming at various spatial scales: Evidence from the Guangdong-Hong Kong-Macau region, China. *Geophysical Research Letters*, *47*(20), e2020GL089152. https://doi.org/10.1029/2020gl089152

Chen, S., & Coauthors. (2021). Study on the seasonal variation of Aeolus detection performance over China using ERA5 and radiosonde data. *Atmospheric Chemistry and Physics Discussions*, 640. https://doi.org/10.5194/acp-2021-298

Chen, T.-C., Huang, W.-R., & Yen, M.-C. (2011). Interannual variation of the late spring–early summer monsoon rainfall in the northern part of the South China Sea. *Journal of Climate*, *24*(16), 4295–4313. https://doi.org/10.1175/2011jcli3930.1

Chen, Y., Luo, Y., & Liu, B. (2022). General features and synoptic-scale environments of mesoscale convective systems over South China during the 2013–2017 pre-summer rainy seasons. *Atmospheric Research*, *266*, 105954. https://doi.org/10.1016/j.atmosres.2021.105954

Chen, Y., Zhang, A., Liu, T., & Li, W. (2024). Diurnally propagating precipitation features caused by MCS activities during the pre-summer rainy season in South China. *Journal of the Meteorological Society of Japan. Ser. II*, *102*(3), 391–406. https://doi.org/10.2151/jmsj.2024-019

Coniglio, M. C., Corfidi, S. F., & Kain, J. S. (2011). Environment and early evolution of the 8 May 2009 derecho-producing convective system. *Monthly Weather Review*, *139*(4), 1083–1102. https://doi.org/10.1175/2010mwr3413.1

Dial, G. L., Racy, J. P., & Thompson, R. L. (2010). Short-term convective mode evolution along synoptic boundaries. *Weather and Forecasting*, *25*(5), 1430–1446. https://doi.org/10.1175/2010waf2222315.1

Ding, Y. (1992). Summer monsoon rainfalls in China. *Journal of the Meteorological Society of Japan. Ser. II*, *70*(1B), 373–396. https://doi.org/10.2151/jmsj1965.70.1b_373

Du, Y., & Chen, G. (2019). Heavy rainfall associated with double low-level jets over southern China. Part II: Convection initiation. *Monthly Weather Review*, *147*(2), 543–565. https://doi.org/10.1175/mwr-d-18-0102.1

Du, Y., Chen, G., Han, B., Bai, L., & Li, M. (2020). Convection initiation and growth at the coast of South China. Part II: Effects of the terrain, coastline, and cold pools. *Monthly Weather Review*, *148*(9), 3871–3892. https://doi.org/10.1175/mwr-d-20-0090.1

Du, Y., Chen, G., Han, B., Mai, C., Bai, L., & Li, M. (2020). Convection initiation and growth at the coast of South China. Part I: Effect of the marine boundary layer jet. *Monthly Weather Review*, *148*(9), 3847–3869. https://doi.org/10.1175/mwr-d-20-0089.1

Du, Y., Chen, Y.-L., & Zhang, Q. (2015). Numerical simulations of the boundary layer jet off the southeastern coast of China. *Monthly Weather Review*, *143*(4), 1212–1231. https://doi.org/10.1175/mwr-d-14-00348.1

Du, Y., Zhang, Q., Chen, Y.-l., Zhao, Y., & Wang, X. (2014). Numerical simulations of spatial distributions and diurnal variations of low-level jets in China during early summer. *Journal of Climate*, *27*(15), 5747–5767. https://doi.org/10.1175/jcli-d-13-00571.1

French, A. J., & Parker, M. D. (2010). The response of simulated nocturnal convective systems to a developing low-level jet. *Journal of the Atmospheric Sciences*, *67*(10), 3384–3408. https://doi.org/10.1175/2010jas3329.1

He, Y., Wang, K., & Feng, F. (2021). Improvement of ERA5 over ERA-Interim in simulating surface incident solar radiation throughout China. *Journal of Climate*, *34*(10), 3853–3867. https://doi.org/10.1175/jcli-d-20-0300.1

Hersbach, H., Bell, B., Berrisford, P., Hirahara, S., Horányi, A., Muñoz-Sabater, J., et al. (2020). The ERA5 global reanalysis. *Quarterly Journal of the Royal Meteorological Society*, *146*(730), 1999–2049. https://doi.org/10.1002/qj.3803

Hiris, Z. A., & Gallus, W. A., Jr. (2021). On the relationship of cold pool and bulk shear magnitudes on upscale convective growth in the Great Plains of the United States. *Atmosphere*, *12*(8), 1019. https://doi.org/10.3390/atmos12081019

Houze Jr, R. A. (2004). Mesoscale convective systems. *Reviews of Geophysics*, *42*(4). https://doi.org/10.1029/2004rg000150

Huang, L., & Luo, Y. (2017). Evaluation of quantitative precipitation forecasts by TIGGE ensembles for south China during the presummer rainy season. *Journal of Geophysical Research: Atmospheres*, *122*(16), 8494–8516. https://doi.org/10.1002/2017jd026512

Huffman, G. J., Bolvin, D. T., Braithwaite, D., Hsu, K., Joyce, R., Xie, P., & Yoo, S.-H. (2015). NASA Global Precipitation Measurement (GPM) Integrated Multi-Satellite Retrievals for GPM (IMERG). *Algorithm Theoretical Basis Document (ATBD) Version*, *4*, 2020.

Jiang, Q., Li, W., Fan, Z., He, X., Sun, W., Chen, S., et al. (2021). Evaluation of the ERA5 reanalysis precipitation dataset over Chinese Mainland. *Journal of Hydrology*, *595*, 125660. https://doi.org/10.1016/j.jhydrol.2020.125660

Jiang, Y., Han, S., Shi, C., Gao, T., Zhen, H., & Liu, X. (2021). Evaluation of HRCLDAS and ERA5 datasets for near-surface wind over Hainan Island and South China Sea. *Atmosphere*, *12*(6), 766. https://doi.org/10.3390/atmos12060766

Jiao, D., Xu, N., Yang, F., & Xu, K. (2021). Evaluation of spatial-temporal variation performance of ERA5 precipitation data in China. *Scientific Reports*, *11*, 1–13. https://doi.org/10.1038/s41598-021-97432-y

Li, S., Meng, Z., & Wu, N. (2021). A preliminary study on the organizational modes of mesoscale convective systems associated with warm-sector heavy rainfall in South China. *Journal of Geophysical Research: Atmospheres*, *126*(16), e2021JD034587. https://doi.org/10.1029/2021jd034587

Li, X., Guo, X., & Fu, D. (2013). TRMM-retrieved cloud structure and evolution of MCSs over the northern South China Sea and impacts of CAPE and vertical wind shear. *Advances in Atmospheric Sciences*, *30*(1), 77–88. https://doi.org/10.1007/s00376-012-2055-2

Li, Z., Luo, Y., Du, Y., & Chan, J. C. (2020). Statistical characteristics of pre-summer rainfall over South China and associated synoptic conditions. *Journal of the Meteorological Society of Japan. Ser. II*, *98*(1), 213–233. https://doi.org/10.2151/jmsj.2020-012

Liu, B., Guo, J., Gong, W., Zhang, Y., Shi, L., & Ma, Y. (2021). Intercomparison of wind observations from ESA's satellite mission Aeolus, ERA5 reanalysis and radiosonde over China. *Atmospheric Chemistry and Physics Discussions*, 1–35.

Liu, L., Gu, H., Xie, J., & Xu, Y. P. (2021). How well do the ERA-Interim, ERA-5, GLDAS-2.1 and NCEP-R2 reanalysis datasets represent daily air temperature over the Tibetan Plateau? *International Journal of Climatology*, *41*(2), 1484–1505. https://doi.org/10.1002/joc.6867

Liu, B., Guo, J., Gong, W., Zhang, Y., Shi, L., & Ma, Y. (2022). Intercomparison of wind observations from ESA's satellite mission Aeolus, ERA5 reanalysis and radiosonde over China. *Atmospheric Measurement Techniques Discussions*, 1–32.

Liu, X., Luo, Y., Guan, Z., & Zhang, D. L. (2018). An extreme rainfall event in coastal South China during SCMREX-2014: Formation and roles of rainband and echo trainings. *Journal of Geophysical Research: Atmospheres*, *123*(17), 9256–9278. https://doi.org/10.1029/2018jd028418

Luo, Y., Xia, R., & Chan, J. C. (2020). Characteristics, physical mechanisms, and prediction of pre-summer rainfall over South China: Research progress during 2008-2019. *Journal of the Meteorological Society of Japan. Ser., II*.

Mai, C., & Du, Y. (2022). Mesoscale moisture transport in determining the location of daytime convection initiations clustered in time and space over southern China. *Journal of Geophysical Research: Atmospheres*, *127*(11), e2021JD036098. https://doi.org/10.1029/2021jd036098

Meng, Z., Yan, D., & Zhang, Y. (2013). General features of squall lines in East China. *Monthly Weather Review*, *141*(5), 1629–1647. https://doi.org/10.1175/mwr-d-12-00208.1

Mulholland, J. P., Nesbitt, S. W., & Trapp, R. J. (2019). A case study of terrain influences on upscale convective growth of a supercell. *Monthly Weather Review*, *147*(12), 4305–4324. https://doi.org/10.1175/mwr-d-19-0099.1

Parker, M. D. (2021). Self-organization and maintenance of simulated nocturnal convective systems from PECAN. *Monthly Weather Review*, *149*(4), 999–1022. https://doi.org/10.1175/mwr-d-20-0263.1

Schumacher, R. S., & Peters, J. M. (2017). Near-surface thermodynamic sensitivities in simulated extreme-rain-producing mesoscale convective systems. *Monthly Weather Review*, *145*(6), 2177–2200. https://doi.org/10.1175/mwr-d-16-0255.1

Shen, Y., Du, Y., & Chen, G. (2020). Ensemble sensitivity analysis of heavy rainfall associated with three MCSs coexisting over southern China. *Journal of Geophysical Research: Atmospheres*, *125*(2), e2019JD031266. https://doi.org/10.1029/2019jd031266

Song, Y., & Wei, J. (2021). Diurnal cycle of summer precipitation over the North China Plain and associated land–atmosphere interactions: Evaluation of ERA5 and MERRA-2. *International Journal of Climatology*, *41*(13), 6031–6046. https://doi.org/10.1002/joc.7166

Squitieri, B. J., & Gallus, W. A., Jr. (2022). On the changes in convection-allowing WRF forecasts of MCS evolution due to decreases in model horizontal and vertical grid spacing. Part I: Changes in cold pool evolution. *Weather and Forecasting*, *37*(10), 1903–1923. https://doi.org/10.1175/waf-d-22-0041.1

Su, L. (2024). Upscale convective growth at coastal South China [Dataset]. *Zenodo*. https://doi.org/10.5281/zenodo.13788156

Su, L., Sun, X., Du, Y., Fung, J. C., & Chen, G. (2023). The roles of local convergences in the convection initiation of a record-breaking rainfall event at the coastal Pearl River Delta in South China. *Journal of Geophysical Research: Atmospheres*, *128*(3), e2022JD037234. https://doi.org/10.1029/2022jd037234

Tang, W., Qin, J., Yang, K., Zhu, F., & Zhou, X. (2021). Does ERA5 outperform satellite products in estimating atmospheric downward longwave radiation at the surface? *Atmospheric Research*, *252*, 105453. https://doi.org/10.1016/j.atmosres.2021.105453

Thielen, J. E., & Gallus, W. A. (2019). Influences of horizontal grid spacing and microphysics on WRF forecasts of convective morphology evolution for nocturnal MCSs in weakly forced environments. *Weather and Forecasting*, *34*(5), 1495–1517. https://doi.org/10.1175/waf-d-18-0210.1

Trapp, R. J., & Weisman, M. L. (2003). Low-level mesovortices within squall lines and bow echoes. Part II: Their genesis and implications. *Monthly Weather Review*, *131*(11), 2804–2823. https://doi.org/10.1175/1520-0493(2003)131<2804:lmwsla>2.0.co;2

Wang, C., Chen, X., Zhao, K., & Peng, C. H. (2024). Synoptic control on the initiation and rainfall characteristics of warm-season MCSs over the South China Coast. *Journal of Geophysical Research: Atmospheres*, *129*(8), e2023JD039232. https://doi.org/10.1029/2023jd039232

Wang, H., Luo, Y., & Jou, B. J. D. (2014). Initiation, maintenance, and properties of convection in an extreme rainfall event during SCMREX: Observational analysis. *Journal of Geophysical Research: Atmospheres*, *119*(23), 13–232. https://doi.org/10.1002/2014jd022339

Weisman, M. L., & Trapp, R. J. (2003). Low-level mesovortices within squall lines and bow echoes. Part I: Overview and dependence on environmental shear. *Monthly Weather Review*, *131*(11), 2779–2803. https://doi.org/10.1175/1520-0493(2003)131<2779:lmwsla>2.0.co;2

Wu, G., Qin, S., Mao, Y., Ma, Z., & Shi, C. (2022). Validation of precipitation events in ERA5 to gauge observations during warm seasons over eastern China. *Journal of Hydrometeorology*, *23*(5), 807–822. https://doi.org/10.1175/jhm-d-21-0195.1

Xie, W., Yi, S., Leng, C., Xia, D., Li, M., Zhong, Z., & Ye, J. (2022). The evaluation of IMERG and ERA5-Land daily precipitation over China with considering the influence of gauge data bias. *Scientific Reports*, *12*, 1–21. https://doi.org/10.1038/s41598-022-12307-0

Yang, Q., Leung, L. R., Feng, Z., Song, F., & Chen, X. (2021). A simple Lagrangian parcel model for the initiation of summertime mesoscale convective systems over the central United States. *Journal of the Atmospheric Sciences*, *78*, 3537–3558. https://doi.org/10.1175/jas-d-21-0136.1

Zeng, Z., Huang, L., Schultz, D. M., Garcia-Carreras, L., & Wang, D. (2023). Comparing synoptic conditions and environmental characteristics for fronts with and without prefrontal convection initiation and heavy rain over coastal South China. *Monthly Weather Review*, *151*(12), 3235–3254. https://doi.org/10.1175/mwr-d-23-0054.1

Zhang, L., Fu, T. M., Hu, Z., Liu, H., Meng, Z., et al. (2024). Springtime mesoscale convective systems over South China: A historic radar image-based analysis of climatological features, interannual variability, and potential connections with surface aerosol. *Environmental Research Letters*, *19*(2), 024026. https://doi.org/10.1088/1748-9326/ad2024

Zhang, M., Rasmussen, K. L., Meng, Z., & Huang, Y. (2022). Impacts of coastal terrain on warm-sector heavy-rain-producing MCSs in southern China. *Monthly Weather Review*, *150*(3), 603–624. https://doi.org/10.1175/mwr-d-21-0190.1

Zhang, S., Liang, Z., Wang, D., & Chen, G. (2022). Nocturnal convection initiation over inland South China during a record-breaking heavy rainfall event. *Monthly Weather Review*, *150*(11), 2935–2957. https://doi.org/10.1175/mwr-d-21-0264.1

Zhang, W., Zhang, H., Liang, H., Lou, Y., Cai, Y., Cao, Y., et al. (2019). On the suitability of ERA5 in hourly GPS precipitable water vapor retrieval over China. *Journal of Geodesy*, *93*(10), 1897–1909. https://doi.org/10.1007/s00190-019-01290-6

Zhang, Y., Cai, C., Chen, B., & Dai, W. (2019). Consistency evaluation of precipitable water vapor derived from ERA5, ERA-Interim, GNSS, and radiosondes over China. *Radio Science*, *54*(7), 561–571. https://doi.org/10.1029/2018rs006789

Zhang, Z., Varble, A., Feng, Z., Hardin, J., & Zipser, E. (2021). Growth of mesoscale convective systems in observations and a seasonal convection-permitting simulation over Argentina. *Monthly Weather Review*, *149*(10), 3469–3490. https://doi.org/10.1175/mwr-d-20-0411.1

Zhu, L., Bai, L., Chen, G., Sun, Y. Q., & Meng, Z. (2021). Convection initiation associated with ambient winds and local circulations over a tropical island in South China. *Geophysical Research Letters*, *48*(16), e2021GL094382. https://doi.org/10.1029/2021gl094382

Zou, J., Lu, N., Jiang, H., Qin, J., Yao, L., Xin, Y., & Su, F. (2022). Performance of air temperature from ERA5-Land reanalysis in coastal urban agglomeration of Southeast China. *Science of The Total Environment*, *828*, 154459. https://doi.org/10.1016/j.scitotenv.2022.154459